

LONG WAVELENGTH GAS BASED HOT
ELECTRON PHOTOEMISSION DETECTORS

A THESIS

SUBMITTED TO THE DEPARTMENT OF PHYSICS
AND THE INSTITUTE OF ENGINEERING AND SCIENCE
OF BILKENT UNIVERSITY

IN PARTIAL FULFILLMENT OF THE REQUIREMENTS
FOR THE DEGREE OF
MASTER OF SCIENCE

BY

İBRAHİM KİMUKİN

JULY 1999

TK
8300
K56
1999

LONG WAVELENGTH GAAS BASED HOT ELECTRON PHOTOEMISSION DETECTORS

A THESIS

SUBMITTED TO THE DEPARTMENT OF PHYSICS
AND THE INSTITUTE OF ENGINEERING AND SCIENCE
OF BILKENT UNIVERSITY
IN PARTIAL FULFILLMENT OF THE REQUIREMENTS
FOR THE DEGREE OF
MASTER OF SCIENCE

By

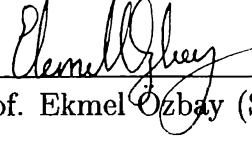
İbrahim Kimukin

July 1999

BC49036

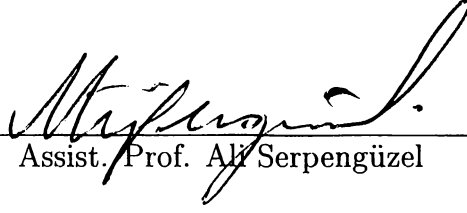
TK
8300
.K56
1938

I certify that I have read this thesis and that in my opinion it is fully adequate, in scope and in quality, as a dissertation for the degree of Master of Science.



Assoc. Prof. Ekmel Özbay (Supervisor)

I certify that I have read this thesis and that in my opinion it is fully adequate, in scope and in quality, as a dissertation for the degree of Master of Science.



Assist. Prof. Ali Serpengüzel

I certify that I have read this thesis and that in my opinion it is fully adequate, in scope and in quality, as a dissertation for the degree of Master of Science.



Assoc. Prof. Orhan Arıkan

Approved for the Institute of Engineering and Science:



Prof. Mehmet Baray

Director of Institute of Engineering and Science

Abstract

LONG WAVELENGTH GAAS BASED HOT ELECTRON PHOTOEMISSION DETECTORS

İbrahim Kimukin

M. S. in Physics

Supervisor: Assoc. Prof. Ekmel Özbay

July 1999

The increasing rate of telecommunication alters both science and technology, and demands high performance components. Photodetectors are essential components of optoelectronic integrated circuits and fiber optic communication systems. A new family of photodetectors offer high performance along with wavelength selectivity: resonant cavity enhanced (RCE) photodetectors.

In this thesis, we present our efforts for design, fabrication and characterization of GaAs/AlGaAs based Schottky photodetectors operating within the first (850 nm) and second (1300 nm) optical communication windows. Epitaxial wafers are designed using transfer matrix method based simulation and are grown with molecular beam epitaxy. The photodetector operating at 840 nm was designed with indium tin oxide (ITO) Schottky layer for high quantum efficiency. The second photodetector is based on internal photoemission, and is compatible with advanced GaAs process technology. Our aim with this design is high speed operation at the second optical communication window. We measured 20 GHz 3-dB bandwidth with 60% quantum efficiency at 840 nm. We expect 50 GHz 3-dB bandwidth with 0.05% quantum efficiency at 1310 nm.

Keywords: Resonant Cavity, Resonant Cavity Enhancement, Schottky photodetector, Internal Photoemission, High Speed, High Quantum Efficiency, Bandwidth-Efficiency Product

Özet

GAAS TEMELLİ UZUN DALGABOYLARINDA ÇALIŞAN SICAK ELEKTRON FOTOEMİSYON DETEKTÖRÜ

İbrahim Kimukin

Fizik Yüksek Lisans

Tez Yöneticisi: Doç. Dr. Ekmel Özbay

Temmuz 1999

İletişim alanındaki hızlı gelişme bilim ve teknolojiyi etkilemekte, ve yüksek performanslı aygıtlara ihtiyaç duymaktadır. Fotodetektörler optoelektronik tümleşik devre ve optiklif iletişim sistemlerinin vazgeçilmez elemanlarıdır. Resonans çınlaç arttırımlı (RCE) fotodetektörler yüksek performansla beraber dalgaboyu seçimini sunmaktadır.

Bu tezde GaAs/AlGaAs temelli, birinci (850 nm) ve ikinci (1300 nm) optiklif iletişim penceresinde çalışan Schottky fotodetektörlerin tasarım, üretim, ve karakterizasyonunu sunmaktayız. Diyot yapılarının tasarımı transfer matris yöntemine dayalı simulasyon ile yapıldı ve moleküler ışın büyütme tekniğiyle büyütüldü. 840 nm de çalışan fotodetektörde kuvantum verimini arttırmak için Schottky tabakası indiyum kalay oksit (ITO) ile büyütüldü. İkinci detektör gelişmiş GaAs prosesine uygun, iç fotoemisyon kullanarak tasarlandı. Bu tasarımkı amacımız yüksek hız ve ikinci optiklif iletişim penceresinde çalışmak idi. Ölçümlerimizde 840 nm de çalışan dedektörde 20 GHz 3-dB bantgenişliği ve % 60 kuvantum verimi elde ettik. 1310 nm de çalışan dedektörde 50 GHz bantgenişliği ve % 0.05 kuvantum verimi beklemekteyiz.

Anahtar

sözcükler: Resonant Çınlaç, Resonant Çınlaç Arttırımı, Schottky Fotodetektör, İç Fotoemisyon, Yüksek Hız, Yüksek Kuvantum Verimi, Hız-verim Çarpımı

Acknowledgement

It is my pleasure to express my deepest gratitude to my supervisor Assoc. Prof. Ekmel Özbay for his guidance, helpful suggestions and fruitful discussions throughout my thesis work. I have not only benefited from his wide spectrum of interest in physics, but also learned a lot from his superior academic personality.

I would like to thank to all members of physics department and advanced research laboratory, especially Necmi Bıyıklı who taught me everything, I know about GaAs processing, Mehmet Bayındır who helped me write this manuscript. I also want to thank Murat Güre who helped me during my semiconductor device processes.

I wish to thank Assoc. Prof. M. Selim Ünlü, Mutlu Gökkavas and Gökhan Ulu of Boston University for their efforts in high speed measurements of our devices.

Contents

Abstract	i
Özet	i
Acknowledgement	i
Contents	i
List of Figures	iv
List of Tables	vi
1 Introduction	1
2 Theoretical Background	4
2.1 Schottky Photodiode Operation	4
2.1.1 Schottky Junction	5
2.1.2 Detector Operation	7
2.1.3 Diode Performance	11
2.2 Internal Photoemission	13
2.3 Resonant Cavity Enhancement	15
2.3.1 RCE Formulation	17
2.3.2 Standing Wave Effect	18
2.3.3 RCE Optimization	19

3	Design	23
3.1	Materials for Photodetectors	23
3.2	Device Simulation	25
3.3	Cavity Design	28
3.4	NIST Sample	30
	3.4.1 Design and Optimization	30
	3.4.2 Reflectivity Characterization	32
3.5	ISU Sample	34
	3.5.1 Design and Optimization	34
	3.5.2 Reflectivity Characterization	35
4	Fabrication	37
4.1	Standard Processes	37
	4.1.1 Cleaving and Wafer Cleaning	37
	4.1.2 Photolithography	38
	4.1.3 Etching	39
	4.1.4 Metalization	41
	4.1.5 Annealing	41
	4.1.6 Plasma Enhanced Chemical Vapor Deposition	42
	4.1.7 Indium Tin Oxide Deposition	42
	4.1.8 Lift-off	42
4.2	Fabrication	43
	4.2.1 Ohmic Contact Formation	43
	4.2.2 Mesa Isolation	43
	4.2.3 Interconnect Metalization	43
	4.2.4 Schottky Contact Formation	44
	4.2.5 Dielectric Deposition	44
	4.2.6 Airpost Formation	44
	4.2.7 Airbridge Metalization	46
	4.2.8 Top Mirror Deposition	46

5	Measurements	48
5.1	IV Measurements	48
5.2	Quantum Efficiency Measurements	49
5.2.1	NIST Sample	50
5.2.2	ISU Sample	52
5.3	High-Speed Measurements	53
5.3.1	NIST Sample	55
5.3.2	ISU Sample	55
6	Achievements and Future Directions	56

List of Figures

2.1	Energy band diagram of a Schottky junction	5
2.2	Photogenerated carriers inside the depletion layer	7
2.3	The carriers generated at $x = x_0$ induce output current as they move across the depletion region	8
2.4	The induced current as a function of time	10
2.5	Expected output current for a uniformly illuminated diode where hole drift velocity is smaller than the electron drift velocity	10
2.6	(a)Schematics of the photodiode circuitry (b)Equivalent circuit model for high frequency analysis	12
2.7	Excitation of an electron in the internal photoemission	13
2.8	Analysis model of an RCE photodetector	16
2.9	QE for different top DBR reflectivities (R_1) for $\alpha d = 0.1$ and $R_2 = 99.99\%$	19
2.10	QE spectrum for different top DBR reflectivities (R_1) for $\alpha d = 0.1$ and $R_2 = 99.99\%$	20
2.11	QE spectrum for different αd with DBR reflectivities $R_1 = 78.9\%$ and $R_2 = 99.99\%$	21
3.1	Electric fields at the interface	26
3.2	Electric field inside a layer	27
3.3	Electric fields outside our structure	28
3.4	Reflectivity of DBRs used in NIST and ISU samples	29
3.5	Epitaxial design of NIST sample	31

3.6	Measured (solid line) and simulated (dotted line) reflectivity of NIST sample	33
3.7	Epitaxial design of ISU sample	34
3.8	Measured (solid line) and simulated (dotted line) reflectivity of ISU sample	35
3.9	Crosssection of ISU sample taken with SEM	36
4.1	Resist profile of normal and image-reversal photolithography . . .	39
4.2	SEM image of wet-etch profile	40
4.3	SEM photograph of an airbridge	45
4.4	Crosssection of an airbridge	45
4.5	Photograph of complete device	47
5.1	Current-Voltage characteristics of ISU sample	49
5.2	Simple diagram of quantum efficiency setup	50
5.3	Experimental (solid line) and theoretical (dotted line) Quantum Efficiency of NIST sample for different top DBR pair number	51
5.4	Experimental (solid line) and theoretical (dotted line) Quantum Efficiency of ISU sample	52
5.5	Simple diagram of high speed setup	53
5.6	Response of the NIST sample	54

Chapter 1

Introduction

“The new era in communications began with the desire of loved ones to stay in touch with GIs scattered across the United States and dozens of countries around the world. That, combined with the government’s military communications need, spawned the habit of ‘reaching out’ by phone” says Amos Joel, who was awarded the National Medal of Technology by the President of the USA in 1993. The invention of the telephone by Alexander Graham Bell lead to an enormous world wide communication market, which earns 1.5 trillion dollar each year. The unexpected demand for calling services during and after the second world war continued and began to strain the most modernized telephone network.

The invention of the first solid-state transistor in 1947, opened the age of computing and communication. In 1960’s researchers developed the first laser. The development of the first commercially feasible optical fiber in 1970’s made the fiber optic communication a promising candidate for telecommunication. In the early 1980’s satellites capable of carrying nearly 100,000 simultaneous calls are used for telephone calls. Demand for the faster, cheaper, and less noisy communication made the first transatlantic undersea fiber-optic telephone cable possible that replaced the copper one that had been installed in 1956. That was the first fiber-optic revolution in telecommunication.

The second revolution came with the introduction of wavelength division multiplexing (WDM). Telephone companies had laid cable containing 24 to 36

fibers with 2.5 Gbit/s rate, many had been reserved as “dark fiber”. But the tremendous traffic has crowded these cables that once seemed so voluminous. In the mid 1990’s, companies began using systems capable of transmitting at four wavelengths, and soon this number increased to eight.

Due to the properties of the commercial silica based fibers, optoelectronic research focused at three wavelengths, where the minimum attenuation occurs.¹ First one is located at 850 nm, which is called the first optical window. GaAs based detectors are usually used for the detection. Local area networks use this window, because of the high loss in this window. The second and the third windows are located at 1310 and 1550 nm respectively. The loss in these wavelengths is much less than the first optical window, hence they are used for long distance fiber optic communication.

Lasers, modulators, photodetectors, optical amplifiers, and optical fibers are the main components of an optical communication system. The optical fiber offers an operation bandwidth up to tens of THz. The research effort in optoelectronics is devoted to fully exploit the fiber bandwidth. This can be possible with high performance components.

Semiconductor based photodiodes demonstrate excellent features to fulfill the requirements of high speed optoelectronic receiver. GaAs is the most studied material for photodetection. GaAs based Schottky and p-i-n detectors have been demonstrated bandwidth capabilities as high as 200 GHz.²⁻⁵ Using low temperature grown GaAs, photodetectors with bandwidths up to 550 GHz have been fabricated.⁷ However, the efficiencies of these detectors have been less than 10%, due to thin absorption layer needed for short transit time.

Resonant cavity enhanced (RCE) photodetectors offer the possibility of overcoming this limitation of bandwidth-efficiency product of conventional photodetectors.²⁰ The RCE photodetectors are based on the enhancement of the optical field inside a Fabry-Perot cavity. This enhancement allows the usage of thinner active layers, which minimizes the transit time without sacrificing the quantum efficiency. RCE detector research is mainly concentrated in three types of detectors; Schottky, p-i-n, and avalanche photodiodes. 100 GHz bandwidth

and 25 GHz bandwidth-efficiency product Schottky diodes have been reported. 46 GHz bandwidth-efficiency product p-i-n photodetector with 92% quantum efficiency has been reported.⁶

Chapter 2 reviews the theory of Schottky diode, its application as photodetector and its current-voltage characteristics. We also examine the transport of carriers, and the high speed design. We also present the theory of internal photoemission, and wavelength dependence of the quantum efficiency in this effect. We conclude that chapter with the theory of resonant cavity enhancement (RCE) and present the simulation results of the RCE photodetectors.

Chapter 3 contains detailed description of our simulation technique, design parameters of our photodetectors. We also show comparison of our simulated and measured reflectivities of our molecular beam epitaxy grown samples. A brief list of semiconductor materials used in the photodetector designs in different part of the spectrum is also given.

In chapter 4, we present the standard GaAs processing and techniques. We describe our fabrication steps, and process parameters.

Chapter 5 describes the characterization of the fabricated photodetectors. We discuss the measurement of current-voltage characteristics, quantum efficiency, and high-speed measurements. Also the experimental setup used in these measurements are explained and the comparison between the simulations and the measurements is given.

In chapter 6, we present our results, and the improvements can be made to get better results. We also mention our future plans.

Chapter 2

Theoretical Background

Photodetectors can be classified into two categories: thermal detectors and quantum detectors. Thermal detectors sense the radiation by its heating effect. Thermal detectors have the advantage of wide spectral range and operation at the room temperature, but they are limited as far as speed and sensitivity are concerned. Bolometers, thermistors, pyroelectric detectors are widely used thermal detectors. Operation of quantum detectors depend on the discrete nature of photons which can transfer energy of individual particles (electron and hole) giving rise to a photocurrent. These devices are characterized by very high sensitivity, high speed but limited spectral response. Photoemissive, photovoltaic, and photoconductive detectors are classified in this category. The conductivity change in the photoconductive detectors is proportional to the intensity of the radiation falling on the semiconductor. Rectifying junctions are the basis of the photovoltaic detectors. Under the illumination, the excess carriers created within the semiconductor generate a proportional output current.

2.1 Schottky Photodiode Operation

The theory of rectification in metal-semiconductor junction was developed in 1930;s by W. Schottky who attributed rectification to a space-charge layer in the semiconductor.¹⁰ Schottky photodiodes are widely used for high speed

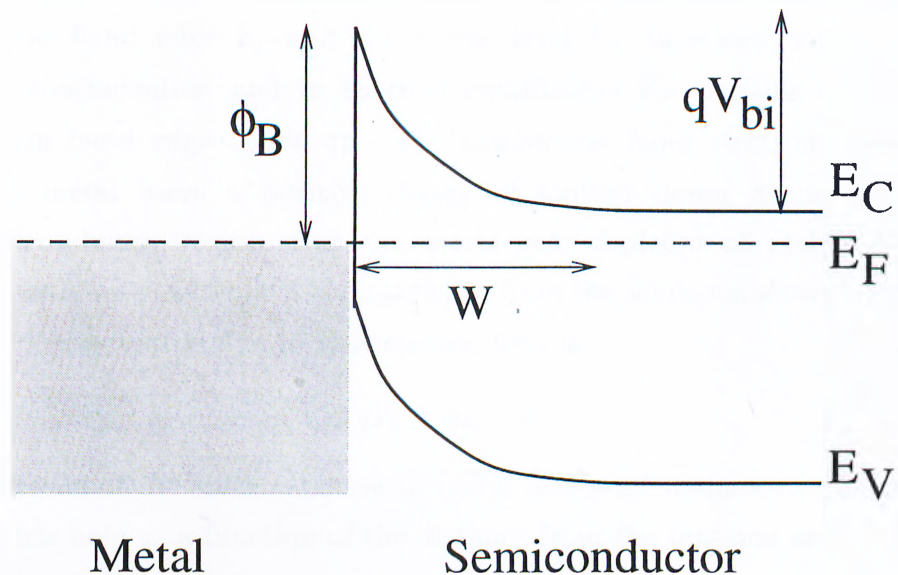


Figure 2.1: Energy band diagram of a Schottky junction

applications.

2.1.1 Schottky Junction

A Schottky diode consists of a metal-semiconductor junction. Figure 2.1 shows the energy band diagram after the contact is made and equilibrium has been reached. When the two substances are brought into intimate contact electrons from the conduction band of the semiconductor, which have higher energy than the electrons in the metal, flow into the metal. This process continues until the Fermi level on both sides is brought into coincidence. As the electrons move from semiconductor to metal, the free electron concentration in the semiconductor region near the boundary decreases. The length of this region is given by⁸:

$$W = \sqrt{\frac{2\varepsilon}{qN_d}(V_{bi} - V)} \quad (2.1)$$

where ε is the dielectric constant of the semiconductor, N_d is the ionized donor atom density, V_{bi} is the built-in potential in the semiconductor, and the V

is the applied potential to the junction. Since the separation between the conduction band edge E_c and the Fermi level E_F increases with decreasing electron concentration and in thermal equilibrium E_F remains constant, the conduction band edge bends up. The conduction band electrons which cross over the metal leave a positive charge of ionized donor atoms behind, so the semiconductor region near the metal gets depleted of mobile electrons. Consequently an electric field is established from the semiconductor to the metal. The build-in potential due to that electric field is

$$qV_i = \phi_m - \phi_s \quad (2.2)$$

the difference of the work function of metal and semiconductor. The potential and electric field as a function of the distance from the junction are given by:

$$\phi(x) = -\frac{qN_d}{2\epsilon} W^2 \left(1 - \frac{x}{W}\right)^2 \quad (2.3)$$

$$E(x) = -\frac{d\phi(x)}{dx} = -\frac{qN_d}{\epsilon} W \left(1 - \frac{x}{W}\right) \quad (2.4)$$

The current transport in the metal-semiconductor contacts is mainly due to majority carriers, in contrast to p-n junctions. There are four different mechanisms by which the carrier transport can occur: (1) thermionic emission over the barrier, (2) tunneling through the barrier, (3) carrier recombination (or generation) in the depletion region, and (4) carrier recombination in the neutral region of the semiconductor. Usually the first process is the dominant mechanism in Schottky barrier junctions in Si and GaAs and leads to the ideal diode characteristics.

Thermionic emission theory is derived by Bethe⁹ for high-mobility semiconductors, and diffusion theory is derived by Schottky¹⁰ for low-mobility semiconductors. A synthesis of the thermionic emission and diffusion approaches has been proposed by Crowell and Sze.¹¹ The complete expression of the J-V characteristics is given by:

$$J = J_s (e^{qV/kT} - 1) \quad (2.5)$$

$$J_s = A^{**} T^2 \exp\left(-\frac{q\phi_{Bn}}{kT}\right) \quad (2.6)$$

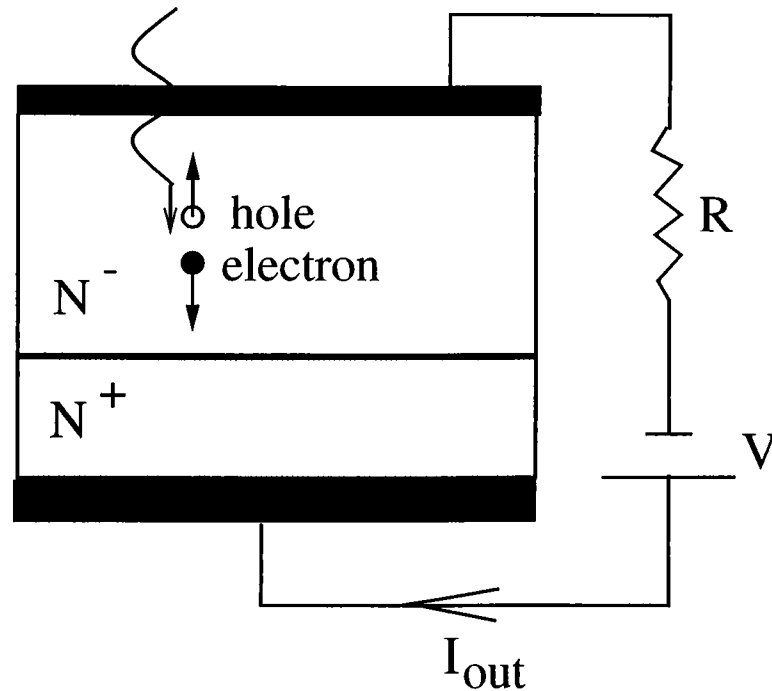


Figure 2.2: Photogenerated carriers inside the depletion layer

where A^{**} is the effective Richardson constant.

2.1.2 Detector Operation

When a reverse bias is applied to the device, as shown in Figure 2.2, the voltage drop across the depletion region increases. This additional voltage drop results in a wider depletion region, and a continuous electric field across the N- region. When a photon with wavelength λ , whose energy is larger than the bandgap, is absorbed in the depletion region an electron hole pair is generated. These carriers are swept away by the electric field,

The number of electrons generated per incident photon is defined as the quantum efficiency, which is expressed as¹²:

$$\eta = \frac{I_p/q}{P_{opt}/h\nu} \quad (2.7)$$

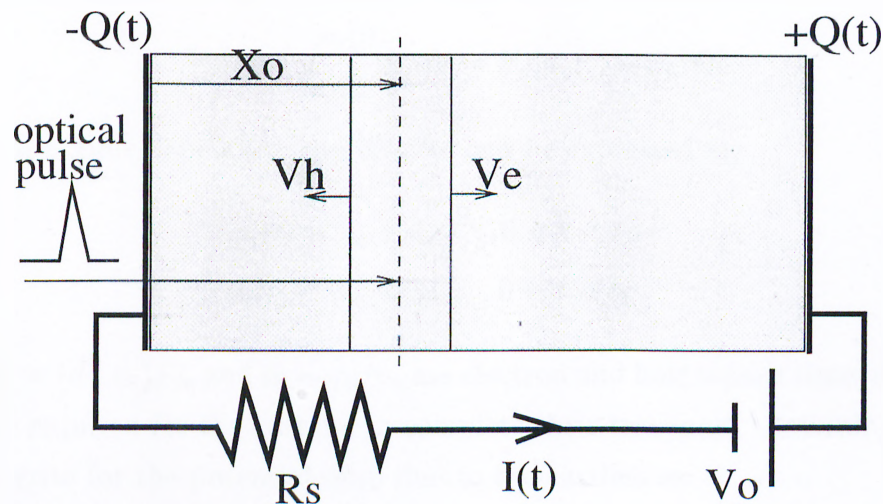


Figure 2.3: The carriers generated at $x = x_0$ induce output current as they move across the depletion region

where I_p is the photo-generated current, P_{opt} is the optical power at frequency ν . The depletion region can be described as a parallel plate capacitor, with area A , width d , and dielectric constant ϵ . At steady state, the voltage across the capacitor is V_0 , which results in a total charge $Q_0 = CV_0$.

Let's assume that, at time $t = 0$, a narrow optical pulse generates carriers with a total charge of q , at a distance x_0 from the Schottky contact, as shown in Figure 2.3. Due to the built-in electric field in the depletion layer, the positive and negative charges are pulled in opposite directions, forming charged sheets with a surface charge density $\sigma = q/A$. The negatively charged sheet corresponds to electrons moving away from the Schottky contact with drift velocity v_e , and positively charged sheet corresponds to holes moving towards the Schottky contact with drift velocity v_h . Each sheet contributes to the electric field formed between the sheets:

$$E_\sigma = \frac{\sigma}{\epsilon} \quad (2.8)$$

The direction of this electric field is opposite to the depletion layer electric field, which results in a voltage drop across the depletion layer as the charges move

away from each other. This time dependent voltage is expressed as¹³:

$$V_{\sigma}(t) = \int_{x_h(t)}^{x_e(t)} E_{\sigma} dx = E_{\sigma}[x_e(t) - x_h(t)] \quad (2.9)$$

where these time dependent coordinates can be expressed as:

$$x_e(t) = x_0 + v_e t \quad , 0 < t < t_e \quad (2.10)$$

$$x_h(t) = x_0 - v_h t \quad , 0 < t < t_h \quad (2.11)$$

where $t_e = (d-x_0)/v_e$ and $t_h = x_0/v_h$ are electron and hole transit time, defined as the time required for the carriers to complete their transport. Assuming $t_e > t_h$, we can write for the potential drop due to the carriers as:

$$V_{\sigma}(t) = \begin{cases} \frac{\sigma}{\epsilon}(v_e + v_h)t & , 0 < t < t_h \\ \frac{\sigma}{\epsilon}v_e t & , t_h < t < t_e \end{cases} \quad (2.12)$$

We can write the output current $I_{out}(t)$ as:

$$I_{out}(t) = \frac{dQ(t)}{dt} = \frac{d}{dt}[CV(t)] \quad (2.13)$$

where $V(t) = V_0 - V_{\sigma}(t)$, so the time dependent current is:

$$I_{out}(t) = \begin{cases} I_1 = \frac{q}{d}(v_e + v_h) & , 0 < t < t_h \\ I_2 = \frac{q}{d}v_e & , t_h < t < t_e \end{cases} \quad (2.14)$$

This time dependent expression is plotted in Figure 2.4.

We can use the same formalism to obtain the output of different cases. In one case, we assume that the absorption over the depletion layer is constant, and the hole drift velocity is smaller than the electron drift velocity, $v_e > v_h$. In this case, when all the electrons reach the end of the depletion layer, there exist some holes that contribute to the total current. So the current flows until all the holes leave the depletion layer. Current output of such a device is shown on Figure 2.5. Another case is that, the absorption constant is so high that all the light is absorbed near the Schottky contact. In this case the current output is a square that continues until t_e .

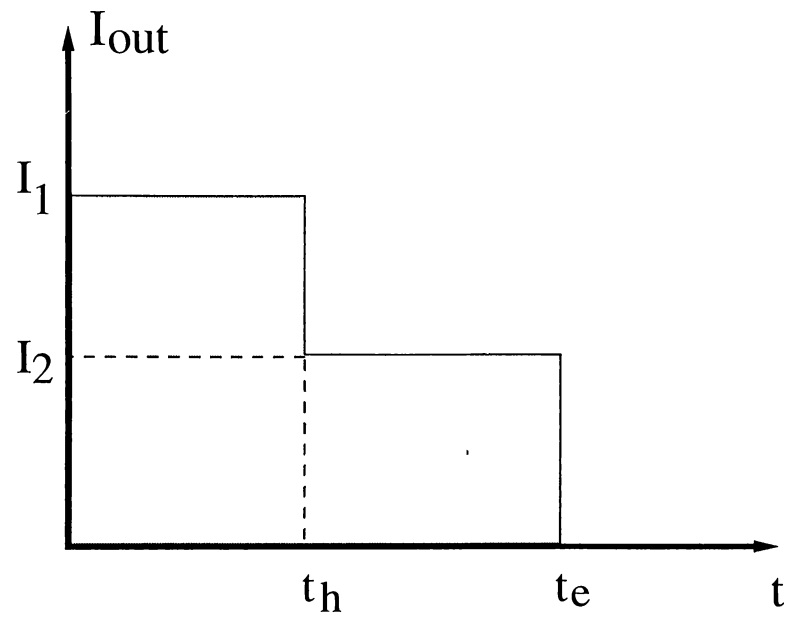


Figure 2.4: The induced current as a function of time

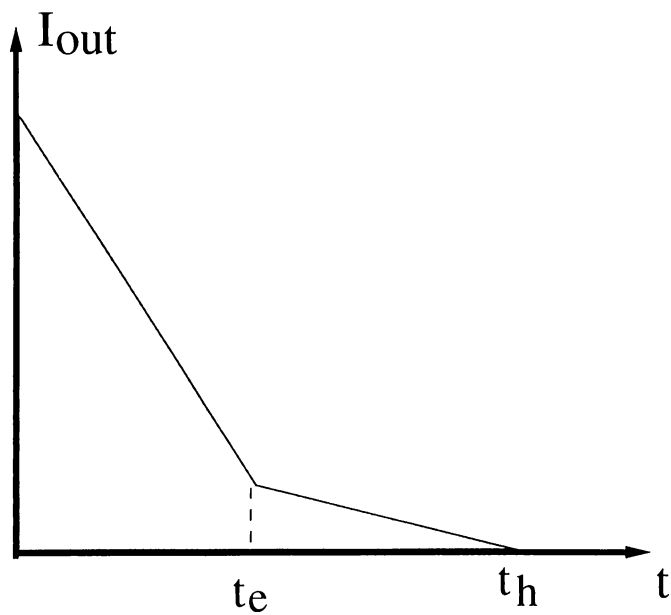


Figure 2.5: Expected output current for a uniformly illuminated diode where hole drift velocity is smaller than the electron drift velocity

2.1.3 Diode Performance

One of the important parameter that reflects the performance of a photodetector is the quantum efficiency, η . For classical photodetectors the expression for the quantum efficiency is given by,

$$\eta = (1 - R)(1 - e^{-\alpha d}) \quad (2.15)$$

where R is the reflectivity of the front surface, α is the power absorption coefficient and d is the thickness of the absorbing layer. So to maximize the quantum efficiency, the surface reflectivity must be minimized, and single pass absorption must be maximized. Reflectivity can be minimized using anti-reflection coatings, and single pass absorption can be maximized by increasing layer thickness.

Another important characteristic is the bandwidth (speed) of the photodiode. The speed is limited by two factors, transit time of the carriers, and the RC time constant of the photodiode.

High frequency analysis can be carried out using the the circuit model in Figure 2.6(b). The photodiode can be modeled by a parallel combination of a current source $I_p(t)$, and a capacitor C_d that represents the capacitance due to the depletion layer. The series resistance of the diode is much smaller than the load impedance, R_L , and is not included in the model.

For the transit time limited case, the 3-dB roll-off frequency can be expressed as:

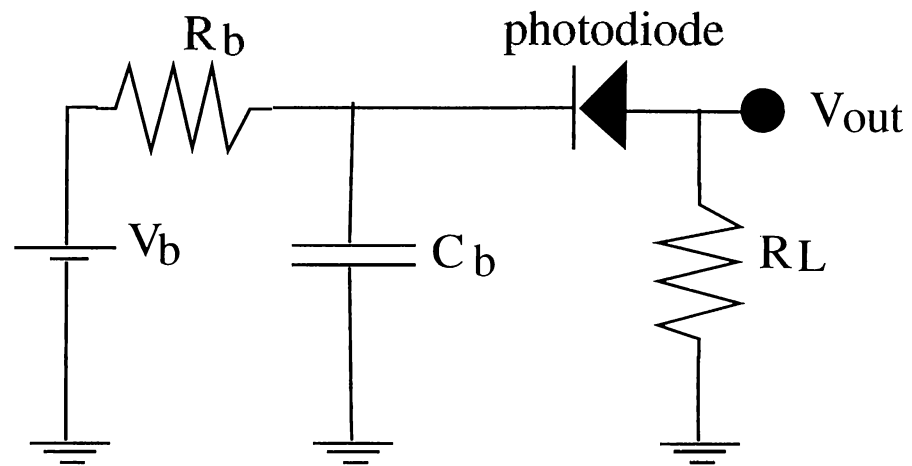
$$f_{tr} = 0.45 \frac{v_e}{d} \quad (2.16)$$

For the RC constant limited case, the 3-dB roll-off frequency is:

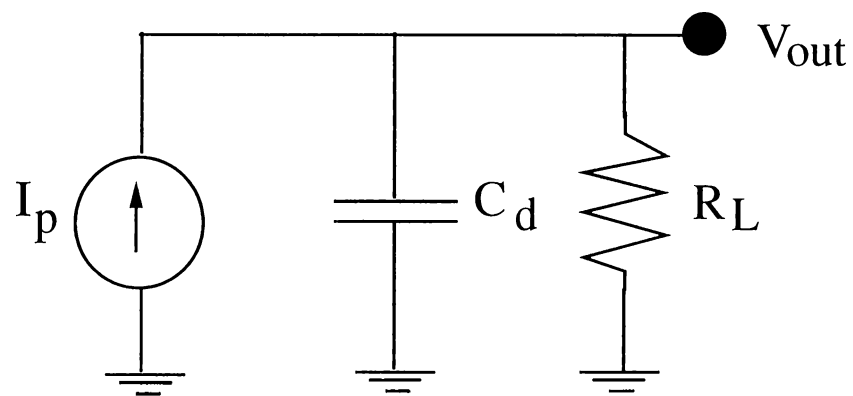
$$f_{RC} = \frac{1}{2\pi R_L C_d} \quad (2.17)$$

The well-known bandwidth-efficiency trade-off is the major blockade for using high speed photodiodes in long-haul telecommunications. As the active layer thickness decreases to minimize the transit time for high speed operation, the quantum efficiency of the same device decreases. For thin active layers, the absorption can be formulated as

$$\eta = (1 - R) \alpha d \quad (2.18)$$



(a)



(b)

Figure 2.6: (a) Schematics of the photodiode circuitry (b) Equivalent circuit model for high frequency analysis

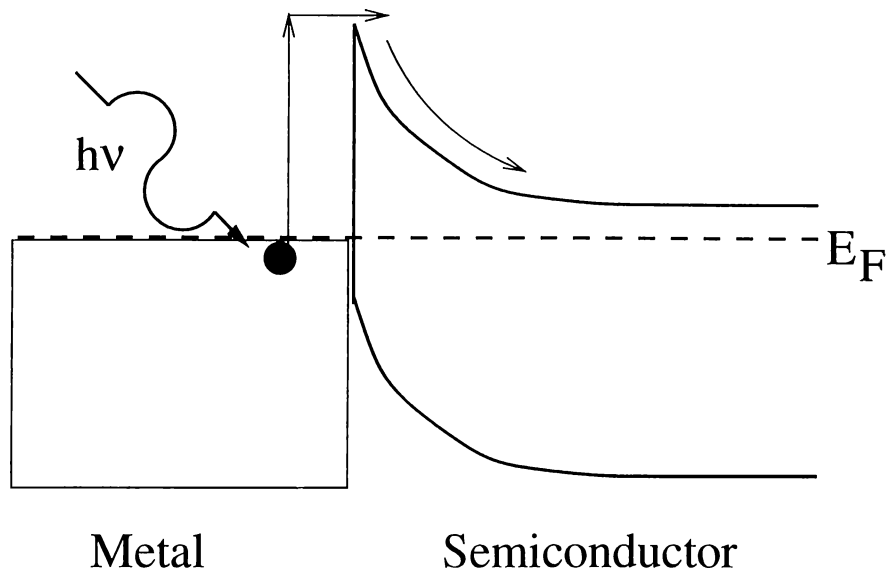


Figure 2.7: Excitation of an electron in the internal photoemission

where $\alpha d \ll 1$ is assumed. Then the bandwidth-efficiency product for a transit time limited photodetector can be obtained as,

$$f_{tr}^{3dB} \cdot \eta = 0.45(1 - R) v_e \alpha \quad (2.19)$$

which is independent of the active layer thickness.

2.2 Internal Photoemission

Schottky diodes are becoming increasingly popular as infrared detectors, despite their low quantum efficiencies relative to other infrared detectors. This is because large format Schottky diode arrays can be fabricated using the same processing procedure as the other integrated circuitry. Iridium silicide Schottky barrier diodes with a cut-off wavelength of more than $10 \mu\text{m}$ have been demonstrated.¹⁴

Internal photoemission corresponds to the optical excitation of electrons in the metal to an energy above the Schottky barrier and then transport to the conduction band of the semiconductor which is shown in Figure 2.7. According to

the theory developed by Fowler, the number of electrons emitted per quantum of light absorbed is to a first approximation proportional to the number of electrons per unit volume of the metal whose kinetic energy normal to the surface is sufficient to overcome the potential step of the surface.¹⁵ We may call the number the number of available electrons.

In a gas of electrons obeying the Fermi-Dirac statistics, the number of electrons per unit volume having velocity component in the range $u + du$, $v + dv$, $w + dw$ is given by the formula:

$$n(u, v, w)dudvdw = 2 \left(\frac{m}{h}\right)^3 \frac{dudvdw}{e^{[\frac{1}{2}m(u^2+v^2+w^2)-E_F]/kT} + 1} \quad (2.20)$$

The number of electrons per unit volume $n(u)du$ with velocity component normal to the surface in the range u , $u + du$ is given by:

$$n(u)du = 2 \left(\frac{m}{h}\right)^3 du \int_0^\infty \int_0^{2\pi} \frac{\rho d\rho d\theta}{e^{[\frac{1}{2}m(u^2+\rho^2)-E_F]/kT} + 1} \quad (2.21)$$

when the integral is taken, we end with an expression:

$$n(u)du = \frac{4\pi kT}{m} \left(\frac{m}{h}\right)^3 \log[e^{(E_F-\frac{1}{2}mu^2)/kT} + 1]du \quad (2.22)$$

As explained before, only the electrons with a total kinetic energy (after absorbing the photon with energy $h\nu$) normal to the interface is larger than $E_F + \phi_B$ can go over the Schottky barrier and contribute to the photocurrent. The number of available electrons is given by:

$$N = \int_{\frac{1}{2}mu^2=E_F+\phi_B-h\nu}^\infty n(u)du \quad (2.23)$$

where $n(u)du$ is given by Eq.(2.20). By making a change of variable $y = (h\nu - \phi_B - E_F + \frac{1}{2}mu^2)/kT$, we obtain:

$$N = \frac{2\pi kT}{m} \left(\frac{2\pi kT}{m}\right)^{1/2} \left(\frac{m}{h}\right)^3 \int_0^\infty \frac{\log[1 + e^{-y+(h\nu-\phi_B)/kT}]}{[y + (E_F + \phi_B - h\nu)/kT]} dy \quad (2.24)$$

To simplify this integral, we consider the region $h\nu$ near ϕ_B . Then, it is a good approximation to neglect y in the denominator of the integral, therefore,

$$N = \frac{2\sqrt{2}}{h^3} \pi m^{3/2} \frac{(kT)^2}{E_F^{1/2}} \int_0^\infty \log[1 + e^{-y+(h\nu-\phi_B)/kT}] dy \quad (2.25)$$

(a) When $\gamma = (h\nu - \phi_B)/kT \leq 0$, the logarithmic term can be expanded, and integrated term by term. Then

$$N = \frac{2\sqrt{2} \pi m^{3/2} (kT)^2}{h^3 E_F^{1/2}} \left[e^\gamma - \frac{e^{2\gamma}}{2^2} + \frac{e^{3\gamma}}{3^2} - \dots \right] \quad (\gamma \leq 0) \quad (2.26)$$

(b) When $\gamma = (h\nu - \phi_B)/kT \geq 0$, the logarithmic term can be expanded, and integrated term by term, giving

$$\int_0^\infty \log[1 + e^{-y+\gamma}] dy = \frac{\pi^2}{6} + \frac{1}{2}\gamma^2 - \left[e^{-\gamma} - \frac{e^{-2\gamma}}{2^2} + \frac{e^{-3\gamma}}{3^2} - \dots \right] \quad (2.27)$$

So:

$$N = \frac{2\sqrt{2} \pi m^{3/2} (kT)^2}{h^3 E_F^{1/2}} \left[\frac{\pi^2}{6} + \frac{1}{2}\gamma^2 - \left(e^{-\gamma} - \frac{e^{-2\gamma}}{2^2} + \frac{e^{-3\gamma}}{3^2} - \dots \right) \right] \quad (\gamma \geq 0) \quad (2.28)$$

We are interested in the situation $\gamma > 0$. Above threshold, for $\gamma > 6$ our expression takes the form

$$N = AT^2\gamma^2 \quad (2.29)$$

with an accuracy of 5%.¹⁶ We can assume that the photoelectric current I per quantum of light absorbed is proportional to N . So for quantum efficiency, we can write:

$$\eta \propto \begin{cases} (h\nu - \phi_B)^2 & , \quad (h\nu > \phi_B) \\ 0 & , \quad (h\nu < \phi_B) \end{cases} \quad (2.30)$$

We derived Eq. 2.30 for bulk material, and didn't take into account the thickness of the Schottky layer. When the reflections from the walls of the metal are taken into account, it has been found that there is an enhancement in the quantum efficiency, but the dependence on the wavelength of the photons is the same.¹⁷⁻¹⁹

2.3 Resonant Cavity Enhancement

For transit time limited photodetectors, the depletion region must be kept thin for the high speed operation. On the other hand, for high quantum efficiency

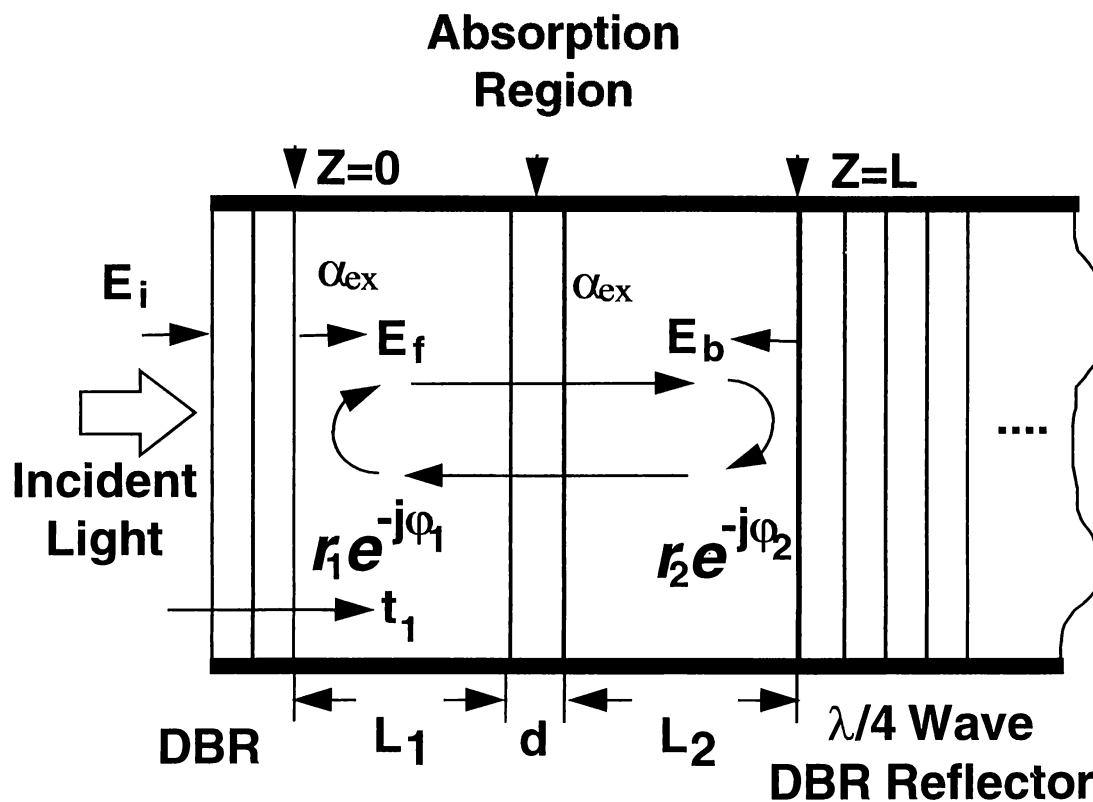


Figure 2.8: Analysis model of an RCE photodetector

the depletion layer must be sufficiently thick to absorb a high fraction of incident light. To overcome this trade off between the response speed and efficiency, we can place a conventional photodetector with a thinner active layer inside a Fabry-Perot microcavity. Thinner active layer results in lower transit time, which increases the performance of the photodetector. This kind of enhancement of the quantum efficiency is called Resonant Cavity Enhancement (RCE). RCE effect was proposed in 1990 and was applied to a broad range of detectors: Schottky,^{36,37} p-i-n,²¹⁻²³ and avalanche^{24,25} photodiodes.

2.3.1 RCE Formulation

Figure 2.8 shows a generalized structure of an RCE photodetector. As the aim is to achieve maximum efficiency, lossless distributed Bragg reflectors (DBR) are used as mirrors of the microcavity. Active layer, where the absorption occurs, is placed between these mirrors. L is the length of the cavity and d is the thickness of the active layer. The field reflection coefficient of the top and bottom reflectors are $r_1 e^{i\phi_1}$ and $r_2 e^{i\phi_2}$, where ϕ_1 and ϕ_2 are phase shifts due to the light penetration into the mirrors. E_i represents the electric field amplitude of the incident light, while E_f is the forward traveling wave at $z = 0$, and E_b is the backward traveling wave at $z = L$. In the cavity, E_f is composed of the transmitted wave from the first mirrors and the reflected wave from the second mirror. Therefore the forward traveling wave, E_f , at $z = 0$ can be obtained in a self-consistent way:

$$E_f = t_1 E_i + r_1 r_2 e^{-\alpha d - \alpha_{ex}(L_1 + L_2)} e^{i(2\beta L + \phi_1 + \phi_2)} E_f \quad (2.31)$$

where $\beta = 2\pi n/\lambda_0$, α and α_{ex} are the absorption coefficients of the active and cavity layers respectively. Solving for E_f gives us

$$E_f = \frac{t_1}{1 - r_1 r_2 e^{-\alpha d - \alpha_{ex}(L_1 + L_2)} e^{-i(2\beta L + \phi_1 + \phi_2)}} E_i \quad (2.32)$$

and backward traveling wave, E_b , at $z = L$ can be expressed as,

$$E_b = r_2 e^{-\frac{\alpha d}{2}} e^{-\frac{\alpha_{ex}}{2}(L_1 + L_2)} e^{-i(\beta L + \phi_2)} E_f. \quad (2.33)$$

The optical power inside the resonant cavity is proportional to the refractive index of the medium and the square of the electric field amplitude.

$$P(z) \propto |E(z)|^2 n \quad (2.34)$$

where $E(z) = E_f(z) + E_b(z)$ is the total electric field. Neglecting the standing wave effect, the power absorbed in the active layer is given by:

$$P_l = \frac{(1 - r_1^2)(e^{-\alpha_{ex} L_1} + r_2^2 e^{-\alpha_{ex} L_2 - \alpha_c L})(1 - e^{-\alpha d})}{1 - 2r_1 r_2 e^{-\alpha_c L} \cos(2\beta L + \phi_1 + \phi_2) + (r_1 r_2)^2 e^{-2\alpha_c L}} P_i \quad (2.35)$$

where $\alpha_c = (\alpha_{ex}(L_1 + L_2) + \alpha d)/L$. Under the assumption that all the photogenerated carriers contribute to the current, η is the ratio of the absorbed power to the incident optical power. i.e., $\eta = P_l/P_i$. Hence:

$$\eta = \left[\frac{(e^{-\alpha_{ex}L_1} + R_2 e^{-\alpha_{ex}L_2} e^{\alpha_c L})}{1 - 2\sqrt{R_1 R_2} e^{-\alpha_c L} \cos(2\beta L + \phi_1 + \phi_2) + R_1 R_2 e^{-\alpha_c L}} \right] (1 - R_1)(1 - e^{-\alpha d}) \quad (2.36)$$

While designing the detector, the cavity layers are chosen such that all the light is absorbed in the active layer ($\alpha_{ex} \ll \alpha$). The expression in the square braces is call the enhancement, as it is the multiplier to the quantum efficiency of a conventional photodiode. Enhancement can be rewritten as:

$$enhancement = \frac{(1 + R_2 e^{\alpha d})}{1 - 2\sqrt{R_1 R_2} e^{-\alpha d} \cos(2\beta L + \phi_1 + \phi_2) + R_1 R_2 e^{-\alpha d}} \quad (2.37)$$

From this expression, it is seen that η is enhanced periodically at the resonant wavelengths of the cavity, $2\beta L + \phi_1 + \phi_2 = 2m\pi$ ($m = 1, 2, 3, \dots$). This term introduces the wavelength selectivity of the RCE effect.

2.3.2 Standing Wave Effect

While deriving Eq.(2.37), the spatial distribution of the optical field inside the cavity was neglected. This spatial distribution arises from the standing wave formed by the two counter propagating waves. This is referred as standing wave effect (SWE).

The SWE is conveniently included in the formalism of η as an effective absorption constant, i.e., $\alpha_{eff} = SWE \times \alpha$. The effective absorption constant α_{eff} is the normalized integral of α and the field intensity across the absorption region.

$$\alpha_{eff} = \frac{\frac{1}{d} \int_0^d \alpha(z) |E(z, \lambda)|^2 dz}{\frac{2}{\lambda} \int_0^{\lambda/2} |E(z, \lambda)|^2 dz} \quad (2.38)$$

When detectors with thick active layers which span several periods of the standing wave are considered, SWE can be neglected. For very thin active layers, which are necessary for strained layer absorbers, SWE must be considered.

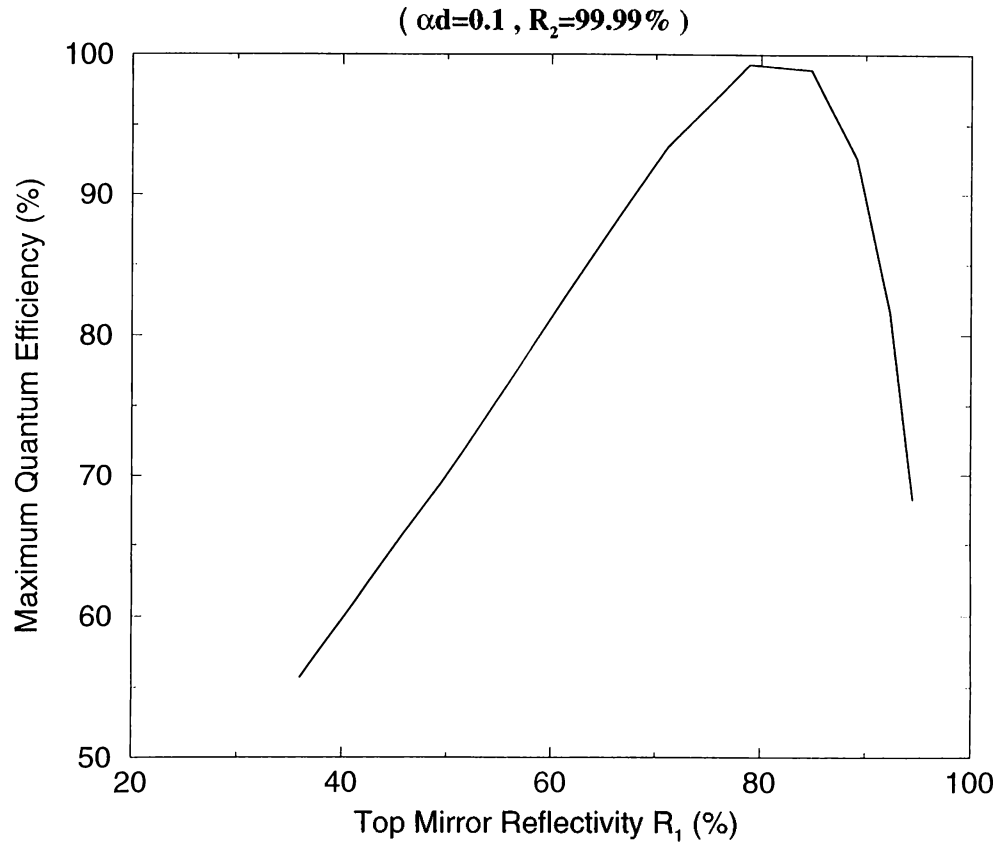


Figure 2.9: QE for different top DBR reflectivities (R_1) for $\alpha d = 0.1$ and $R_2 = 99.99\%$

2.3.3 RCE Optimization

From the expression for the quantum efficiency (η), we see that three parameters R_1 , R_2 , and αd effects η . R_2 , the reflectivity of the bottom mirror, should be designed as high as possible. Else, due to the transmission from the bottom mirror, the performance of the detector decreases dramatically. The other parameter is the reflectivity of the top mirror. When we maximize the quantum efficiency with respect to R_1 , we come up with the condition:

$$R_1 = R_2 e^{-2\alpha d} \quad (2.39)$$

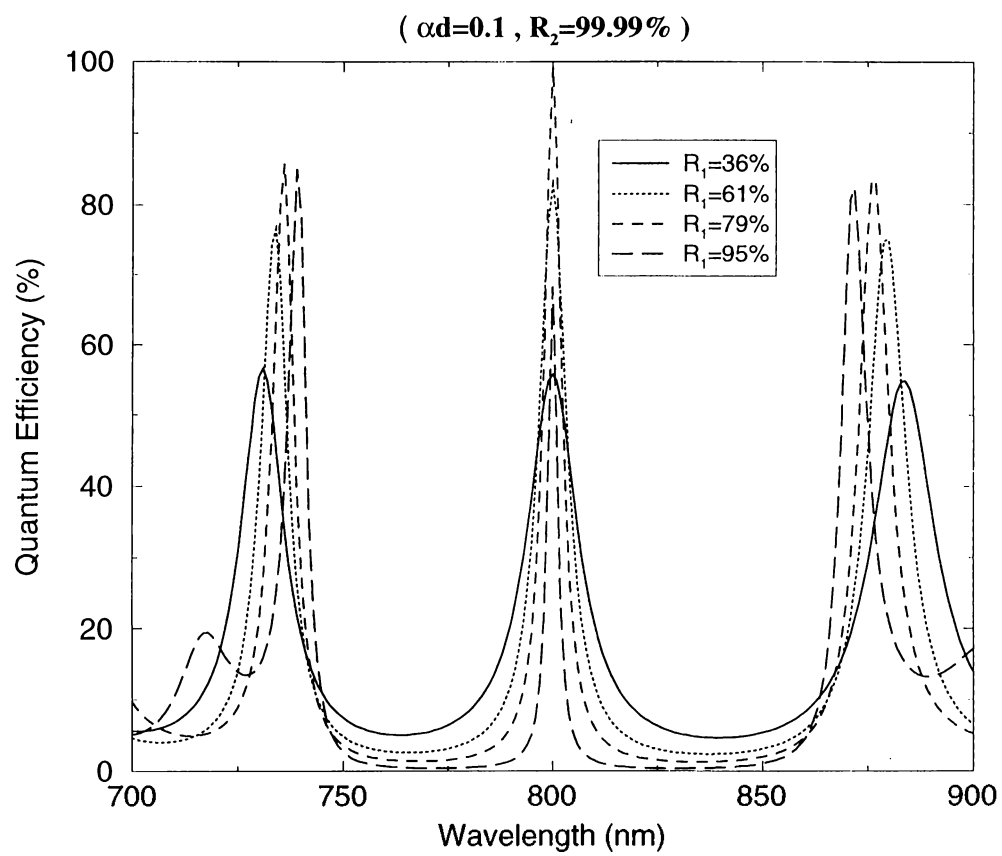


Figure 2.10: QE spectrum for different top DBR reflectivities (R_1) for $\alpha d = 0.1$ and $R_2 = 99.99\%$

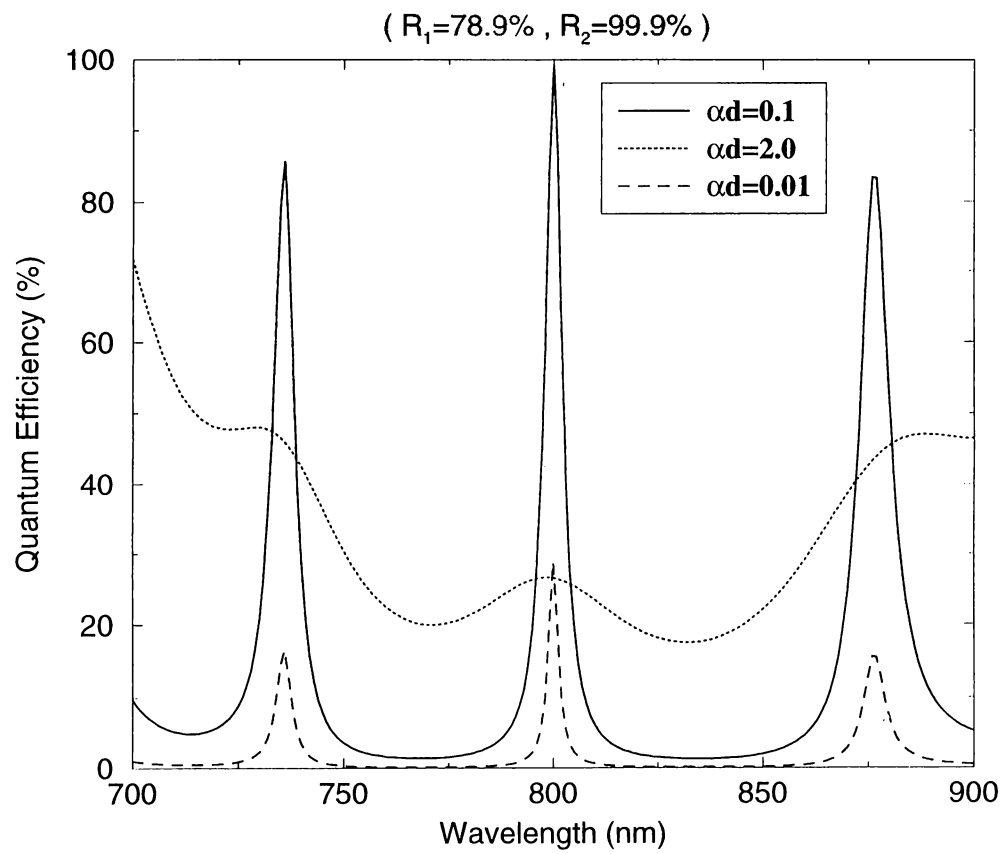


Figure 2.11: QE spectrum for different αd with DBR reflectivities $R_1 = 78.9\%$ and $R_2 = 99.99\%$

The structure used in the simulations consists of 5 pair AlAs/air bottom DBR with a reflectivity of $R_2 = 99.99\%$ at 800 nm and cavity is formed with 950 nm semiconductor with refractive index of 4. Active layer is placed in the center of the layer with $\alpha d = 0.1$. Top DBR consists of Si_3N_4/SiO_2 pairs with a center wavelength $\lambda_c = 800$ nm. As we increase R_1 by increasing the number of Si_3N_4/SiO_2 pairs up to the matching value, $R_1 = 0.81$, the peak quantum efficiency value increases up to 99%, then decreases as shown in Figure 2.9. Figure 2.10 shows the quantum efficiency spectrum, where the full width at half maximum (FWHM) decreases as R_1 increases and the shift in the resonance wavelengths around 740 and 860 nm is due to the penetration of light into the DBR.

Other important parameter for RCE is αd . We simulated for different αd values with $R_1 = 79.0\%$ and $R_2 = 99.9\%$ and the results are presented in Figure 2.11. When αd increases the effect of RCE hence wavelength selectivity, decreases as all the light is absorbed in a single pass without recycling in the cavity.

Chapter 3

Design

In the past 10 years, detector technology has seen a dramatic increase parallel to epitaxial growth technology. New detector materials and structures as well as more complex architectures have become possible to grow. Optical frequencies cover a wide spectrum, from extreme ultraviolet (EUV, $\sim 10\text{nm}$) to far infrared (FIR, $>12\mu\text{m}$). Each spectrum portion has its own applications. UV is used for combustion monitoring, satellite-based missile plume detection, air quality sensing and gas sensing.²⁶ Visible spectrum is used for display, optical storage, and short distance fiber communication. Near infrared contains 1.3 and 1.55 μm , which are the second and third fiber communication windows used for long distance communication.²⁰ IR is used for military applications, remote sensing, gas detection and medical applications.²⁷

3.1 Materials for Photodetectors

The performance of an optical communication system is measured with its bandwidth/cost ratio. To increase this ratio, there is a demand for high performance components, like fibers, lasers, modulators, filters and detectors. It is known that RCE photodiodes offer high-performance with high quantum efficiencies. Features for a proper material system of RCE-detection are very important for a good design:

- Low-loss cavity is very important for limiting the absorption to the active layer
- High-reflectance bottom mirror (DBR) designed with non-absorbing materials increases both quantum efficiency and quality factor of the cavity
- Moderate active layer absorption, αd
- Lattice matched materials must be used to be free from defects

Different material systems can be summarized as below:

- **GaN/ZnSTe** : These materials operate in UV and GaN has many advantages over Si, SiC and Ge which can operate in this wavelength region, but lags in development. GaN, ZnSTe and other nitride based materials eg. AlN, InN are direct bandgap, and they are most promising materials for light-emitting devices in the blue, violet, and ultraviolet region. GaN p- π -n³², Schottky and pn junction photodetectors can be grown on Si,³³ and sapphire,³⁴ whereas high-efficiency ZnSTe photodetectors can be grown on Si, GaAs and GaP.³⁵
- **AlAs/AlGaAs/GaAs** : These materials are grown by MBE very easily, since there is a good lattice match between them. Growth of $\text{Al}_x\text{Ga}_{1-x}\text{As}$ ternary materials enable designs containing graded layers. Since GaAs with a bandgap of 870 nm is used as the active layer, such detectors are used for the first optical communication window. Low-loss or no-loss cavity formation is possible with $\text{Al}_x\text{Ga}_{1-x}\text{As}$ cavity layers and $\text{Al}_x\text{Ga}_{1-x}\text{As}/\text{AlAs}$ pairs for bottom DBR. Unfortunately large number of pairs must be used to get nearly unity reflectivity due to the low refractive index difference of these materials.
- **AlGaAs/GaAs/InGaAs** : InGaAs is used as the active layer in this material system. AlAs has a good lattice match to GaAs, and GaAs/AlAs mirrors can function easily at 1.55 μm . But it is not easy to grow $\text{In}_x\text{Ga}_{1-x}\text{As}$ layers on top of $\text{Al}_x\text{Ga}_{1-x}\text{As}$ due to lattice mismatch. Hence

it is not possible to make a photodiode operating at $1.3 \mu\text{m}$ and $1.55 \mu\text{m}$ with this material system. But high-performance RCE photodiodes have been demonstrated at 900 nm .^{36,37}

- **InP/InGaAs/InAlAs** : When InP used as substrate, the $\text{In}_{0.53}\text{Ga}_{0.47}\text{As}/\text{In}_{0.52}\text{Al}_{0.48}\text{As}$ system grows lattice matched, and their electrical properties and ability to operate between $1.3 \mu\text{m}$ and $1.55 \mu\text{m}$ makes them most appropriate materials in this region. One disadvantage is the poor refractive index contrast between InGaAs and InAlAs. To overcome this GaAs/AlAs mirrors can be wafer-fused to form the microcavity.
- **Si/Ge** : Operation region starts from UV, and extend their range to visible. Ge can operate up to $1.8 \mu\text{m}$. Wide band-gap silicon carbide (SiC) with advanced stage of development seems to be the most suitable material for high-temperature, high-power devices. Si/SiGe DBR for Si and AlAs/GaAs DBR for Ge can be used. The only disadvantage of these materials is that they are indirect bandgap materials.
- **Hg_xZn_{1-x}Te/InSb/InAs** : These materials can operate in the IR region. HgZnTe has been grown in mid 80's, but its growth difficulty has limited its applicability. But in 90's InTlSb has been grown successfully. At these wavelength HgCdTe is still dominant because of its advanced growth technology. By changing Hg concentration in $\text{Hg}_x\text{Zn}_{1-x}\text{Te}$, detection can be extended beyond $15 \mu\text{m}$.

3.2 Device Simulation

Our detector designs, like other RCE photodetectors and VCSELs, are quite complicated and difficult -also very expensive- to grow. Optical properties of materials used in the growth are wavelength dependent and this makes rather difficult to predict the optical field in such multilayer devices, therefore we need

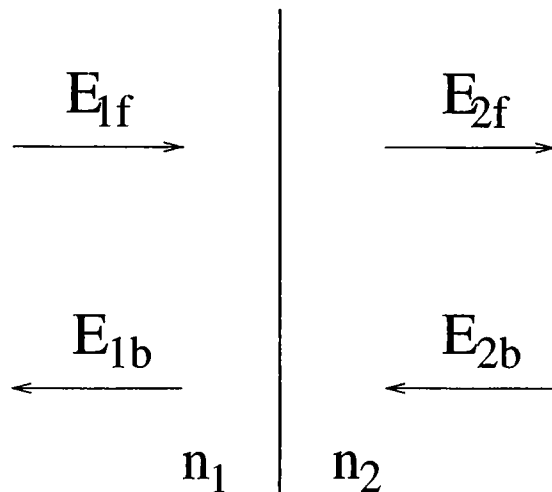


Figure 3.1: Electric fields at the interface

a good simulation method for the analysis before ordering the structure for MBE growth. We used transfer matrix method (TMM), which provides a simple technique to calculate electric and magnetic field distributions inside the cavity.

When we model a layer from an optical point of view, we notice that it consists of two elements; an interface where an abrupt refractive index difference occurs, and a slab where refractive index is constant and extends for a certain width. Refractive index is defined as the square root of the dielectric constant of the medium ; $n = \sqrt{\epsilon - i\epsilon'}$. Imaginary part of the dielectric constant is due to the absorption in the medium, and refractive index can be simplified as $n = n_{real} - in_{imag}$, where both n_{real} and n_{imag} are real and positive numbers.

Electric fields at the left and right of the interface as defined in Figure 3.1 can be related to each other using continuity of the electric and magnetic fields, and given as:

$$\begin{bmatrix} E_{1f} \\ E_{1b} \end{bmatrix} = \frac{1}{t_1} \begin{bmatrix} 1 & r_1 \\ r_1 & 1 \end{bmatrix} \begin{bmatrix} E_{2f} \\ E_{2b} \end{bmatrix} \quad (3.1)$$

where $r_1 = (n_1 - n_2)/(n_1 + n_2)$ and $t_1 = (2n_1)/(n_1 + n_2)$. The electric field inside

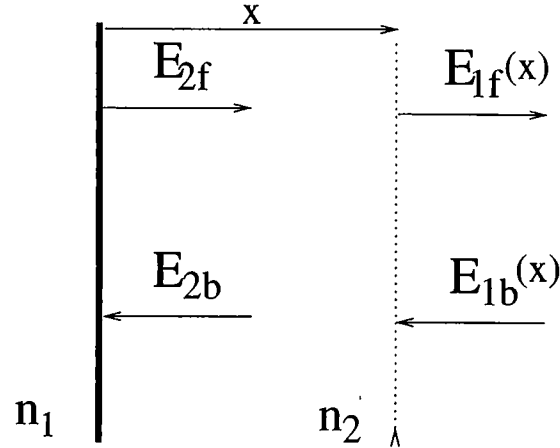


Figure 3.2: Electric field inside a layer

the layer (Figure 3.2) can be found by using the propagation of plane wave:

$$\begin{bmatrix} E_{2f}(x) \\ E_{2b}(x) \end{bmatrix} = \begin{bmatrix} e^{-ikx} & 0 \\ 0 & e^{ikx} \end{bmatrix} \begin{bmatrix} E_{2f} \\ E_{2b} \end{bmatrix} \quad (3.2)$$

where $k = (2\pi n)/\lambda$. When we choose x to be equal to the width of the layer, we can evaluate the electric field just at the left of the next interface. So combining two matrices used in Eq.(3.1) and Eq.(3.2), we can define a transfer matrix for m th layer as:

$$S_m = \frac{1}{t_m} \begin{bmatrix} e^{i\delta_m} & r_m e^{i\delta_m} \\ r_m e^{-i\delta_m} & e^{-i\delta_m} \end{bmatrix} \quad (3.3)$$

where $r_m = (n_m - n_{m+1})/(n_m + n_{m+1})$, $t_m = (2n_m)/(n_m + n_{m+1})$, and $\delta_m = k_m d_m$. Cascading these matrices for N layers, total transfer matrix for the multilayer system is constructed as:

$$S_{total} = S_0 S_1 \cdots S_{N-1} S_N \quad (3.4)$$

So the relation between the electric field at the left and at the right sides of our system as depicted in Figure 3.3 is given by:

$$\begin{bmatrix} E_{bf} \\ E_{bb} \end{bmatrix} = S_{total} \begin{bmatrix} E_{af} \\ E_{ab} \end{bmatrix} \quad (3.5)$$

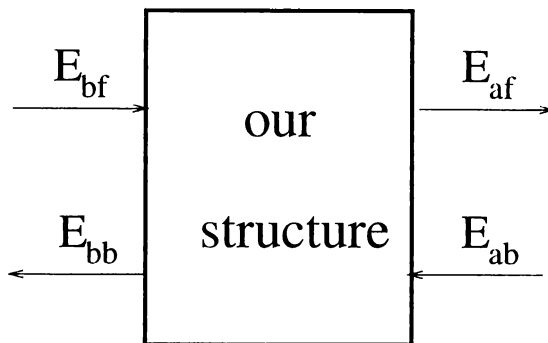


Figure 3.3: Electric fields outside our structure

When we make a measurement like reflectivity, we measure the reflected power not the electric field. The same is valid for the transmittivity and absorption. We can find the power associated with a plane wave using

$$\vec{S} = \frac{1}{\mu} \vec{E} \times \vec{B} \quad (3.6)$$

and using

$$\vec{B} = \frac{1}{\omega} \vec{k} \times \vec{E} \quad (3.7)$$

we find that the power is proportional to the square of the electric field and the refractive index of the medium. Then the reflectivity and the transmittivity are given by:

$$R = \frac{|E_{bb}|^2}{|E_{bf}|^2} \quad (3.8)$$

$$T = \frac{|E_{af}|^2 n_{final}}{|E_{bf}|^2 n_{incidence}} \quad (3.9)$$

Absorption at any layer is found by finding the difference between the power getting into the medium and the power getting out of the medium.

3.3 Cavity Design

As shown in the previous chapter, our aim is to place the active layer inside a cavity formed by two mirrors. Our designs require bottom mirrors with high

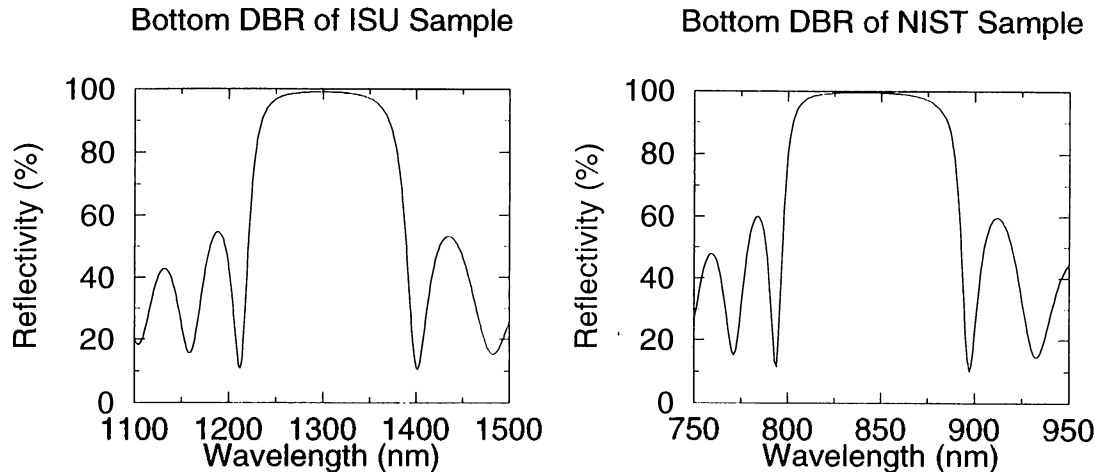


Figure 3.4: Reflectivity of DBRs used in NIST and ISU samples

reflectivities. Although metals are good reflectors, their reflectivities ($R \leq 96$ for thick layers) are not high enough, and change with the spectrum. One of the main disadvantages of metal mirrors is that they are good absorbers at the optical wavelengths, so very thin layers must be used.

Distributed Bragg reflectors (DBR's) are widely used in optoelectronic applications such as detectors and semiconductor lasers. A DBR is a periodic stack with two alternating quarter-wave thick materials with different optical properties. Each pair consist of two layers with refractive indices n_1 and n_2 , and layer thicknesses of $\lambda_c/4n_1$ and $\lambda_c/4n_2$ respectively. λ_c is the central wavelength of the mirror where reflectivity is maximum.

When we observe the light reflected from different interfaces of one pair, we see that all are at the same phase resulting in a constructive interference hence increasing the reflectivity. Applying TMM for a DBR at center wavelength λ_c , results in a simple expression for the reflectivity as

$$R_{max} = \left(\frac{n_1^{2N} - n_2^{2N}}{n_1^{2N} + n_2^{2N}} \right)^2 \quad (3.10)$$

where N is the number of mirror pairs in the stack. For large values of N

reflectance approaches unity, and for a fixed N reflectivity increases as n_2/n_1 increases. %99.6 reflectivity has been achieved with only 2.5 pairs of InP/Air DBR, where as the same reflectivity can be achieved with 51 pair InGaAsP/InP DBR.²⁸ Si/SiO₂ is another material system that can be used with Si based devices.

With a small change in the design of the DBRs, the nature of these mirrors can be changed. If the width of one of the layers (with a refractive index of n_1) increased from $\lambda_c/4n_1$ to $\lambda_c/2n_1$, the structure becomes transparent around λ_c , while still reflecting other wavelengths. In this case, the multilayer stack functions as a filter. Such filters have been demonstrated at various wavelengths on both silicon and GaAs based devices.²⁹⁻³¹

3.4 NIST Sample

This sample is grown in the National Institute of Standard and Technology (NIST) by molecular beam epitaxy (MBE) technique. Epitaxial design of NIST sample is shown in Figure 3.5.

3.4.1 Design and Optimization

Although semitransparent gold Schottky contact is a good top mirror, it absorbs and scatters a large fraction of light. Instead of metals, indium tin oxide (ITO), cadmium tin oxide (CTO) have been studied as Schottky material for MSM devices, photodetectors, LEDs, and solar cells.³⁸⁻⁴² In fact ITO is a highly degenerate n-type semiconductor, that has electrical resistivity of $2-4 \times 10^{-4} \Omega\text{cm}$.⁴³ ITO is a wide gap material (3.3-3.4 eV) that shows high transmission in the visible and near-IR regions of the spectrum. Electrical, optical and structural properties of this material strongly depend on the deposition conditions. We grow ITO layer using magnetron sputtering in the Ar plasma. Our ellipsometer measurements of ITO yielded a refractive index of 2.0, which is in good agreement with the values reported in literature. Several deposition techniques have been used to grow ITO films including chemical

80 nm	$\text{Al}_{0.15}\text{Ga}_{0.85}\text{As}$	N-
30 nm	Graded Region	N-
120 nm	GaAs	N-
30 nm	Graded Region	N-
160 nm	$\text{Al}_{0.2}\text{Ga}_{0.8}\text{As}$	N-
400 nm	$\text{Al}_{0.2}\text{Ga}_{0.8}\text{As}$	N+
230 nm	$\text{Al}_{0.2}\text{Ga}_{0.8}\text{As}$	Undoped
100 nm	$\text{Al}_{0.2}\text{Ga}_{0.8}\text{As}$	N-
19 pair $\text{Al}_{0.2}\text{Ga}_{0.8}\text{As}$ / AlAs DBR		
Semi-Insulating GaAs		

Figure 3.5: Epitaxial design of NIST sample

vapor deposition, magnetron sputtering, evaporation and pulsed laser deposition (PLD). According to the atomic force microscopy measurements, root-mean-square surface roughness of magnetron sputtered films is ~ 40 Angstroms where PLD films is ~ 5 Angstroms.³⁸

The design wavelength of NIST photodiode is 840 nm, so that it can operate in the first optical communication window. GaAs is used as the active layer, and the thickness is chosen to be 120 nm, which is the half wavelength of the resonance wavelength. When the standing wave effect (SWE) is taken into account, the position of the active layer is not important in this case. Hence, we can make wavelength tuning before the fabrication.

In order to have a low-loss cavity, $\text{Al}_{0.15}\text{Ga}_{0.85}\text{As}$ and $\text{Al}_{0.20}\text{Ga}_{0.80}\text{As}$ are used for immediate cavity materials. Bottom mirror consists of 19 period $\text{AlAs}/\text{Al}_{0.2}\text{Ga}_{0.8}\text{As}$ Bragg mirror designed at 840 nm. 230 nm thick $\text{Al}_{0.2}\text{Ga}_{0.8}\text{As}$ undoped layer is for the mesa isolation. Sharp interfaces cause carrier trapping problems at the interfaces, and graded regions are used to get rid of this problem. 100 nm ITO layer is used as the Schottky layer. To achieve the maximum quantum efficiency, 5 pair $\text{Si}_3\text{N}_4/\text{SiO}_2$ DBR must be deposited as the top mirror.

As another design criteria, electron and hole drift velocities are taken into account. Absorption layer is placed closer to the Schottky contact, and the hole and electron transit lengths are chosen such that the electron and hole transit times are equalized ($t_e = t_h$).

3.4.2 Reflectivity Characterization

Before the fabrication, we measured the reflectivity of the sample. We can deduce useful information about the epitaxial structure of the sample by comparing the reflectivity measurements with the theoretical predictions. After the reflectivity measurements, we found out that there was a 1% deviation from the original epilayer design. By changing the simulation parameter, we made a fit to reflectivity data, that is shown in Figure 3.6 with the reflectivity measurement.

We first fabricated our devices with gold Schottky contact. In this case, we

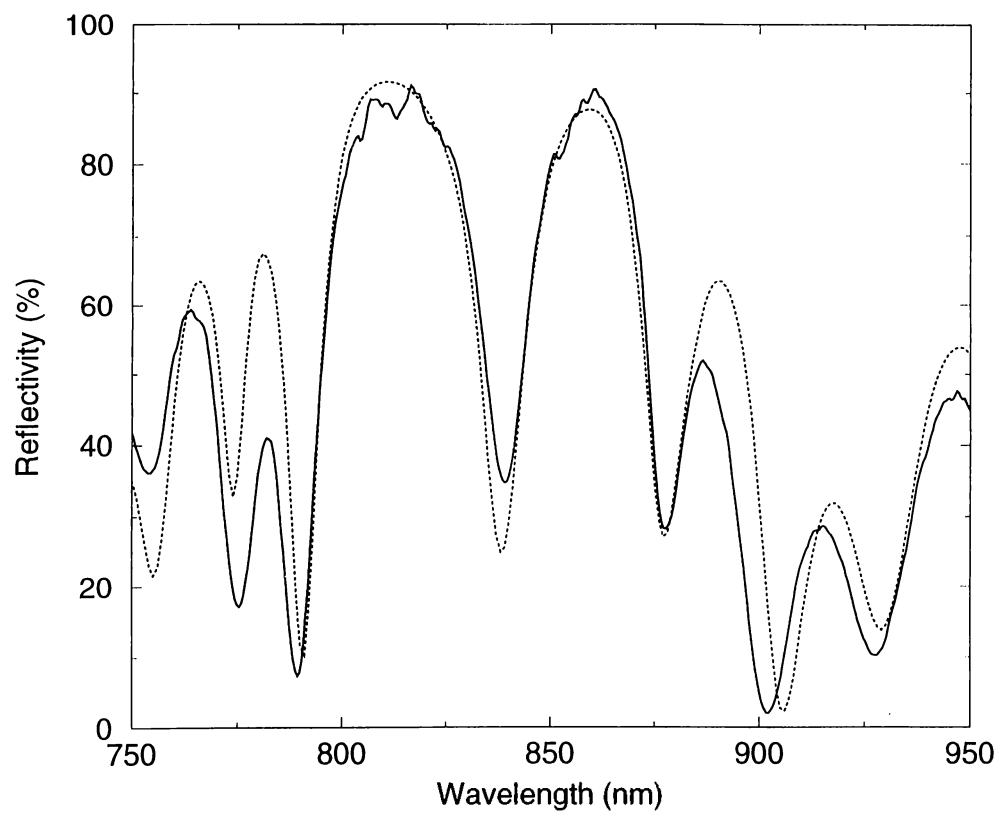


Figure 3.6: Measured (solid line) and simulated (dotted line) reflectivity of NIST sample

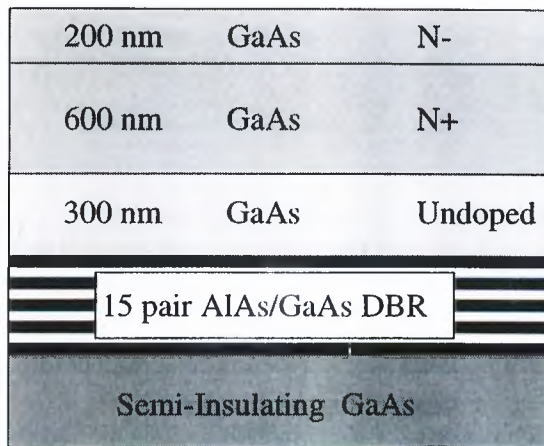


Figure 3.7: Epitaxial design of ISU sample

had to bias the diode to 6 V to deplete the n- layers. Before fabricating with ITO Schottky layer, we decided to recess etch the sample until the n- GaAs layer, to deplete the n- layers at a lower bias.

3.5 ISU Sample

This sample is grown in Iowa State University (ISU) by molecular beam epitaxy (MBE) technique. Epitaxial design of the ISU sample is shown in Figure 3.7.

3.5.1 Design and Optimization

This photodiode is designed to operate at 1.3 μm , so that it can be used for the 2nd optical communication window. It consists of GaAs layers as cavity layers, n- layer is very lightly doped, and n+ region is doped to 10^{18} cm^{-3} for the ohmic contact. Bottom mirror consists of 15 pair AlAs/GaAs DBR centered at 1.3 μm . This mirror has reflectivity greater than 95% between 1244 nm and 1359 nm. Maximum reflectivity of 99% is achieved at 1300nm.

The photons will be absorbed at the gold Schottky layer, and the photo-generated electrons which can travel over the Schottky barrier to the depletion

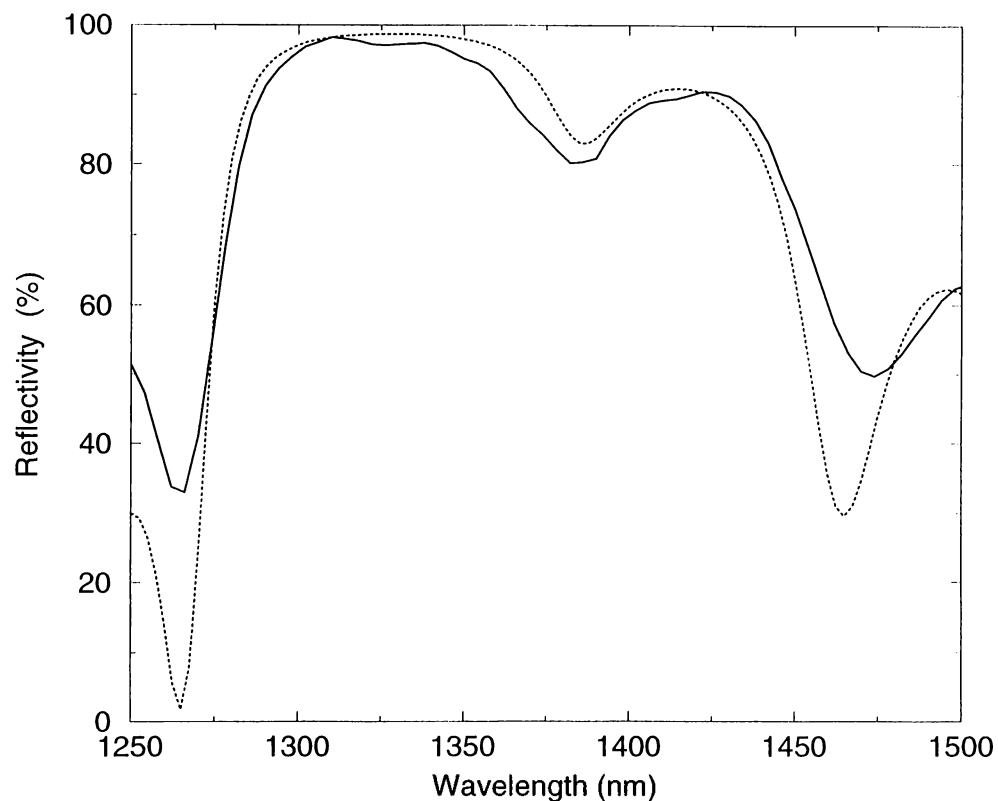


Figure 3.8: Measured (solid line) and simulated (dotted line) reflectivity of ISU sample

layer will be detected. The Au-Schottky barrier has barrier height of 0.8 eV. So signals up to $1.5 \mu\text{m}$ should be detected according to the theory of internal photoemission.

The resonant wavelength of the designed cavity is $1.4 \mu\text{m}$. By etching the top GaAs layer, the resonant wavelength can be tuned to the desired value of $1.3 \mu\text{m}$.

3.5.2 Reflectivity Characterization

Before the fabrication, we measured the reflectivity spectrum of the sample. We fitted the simulation to the reflectivity data by changing the thickness of the layers in the simulation. We found out that there was a 4-6% deviation from the

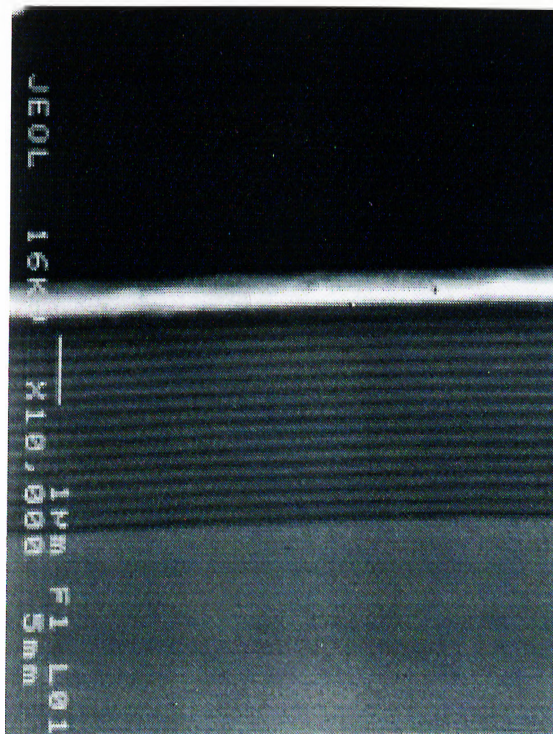


Figure 3.9: Crosssection of ISU sample taken with SEM

original epilayer design. Due to this deviation, the center of the mirror has shifted to $1.37 \mu\text{m}$. Figure 3.8 shows the measured and simulated reflectivity spectrum. Figure 3.9 shows the crosssection of the ISU sample obtained by scanning electron microscopy (SEM). The DBR layers of the ISU sample can be seen as lines with different colors.

The lower edge of the DBR mirror starts at $1.3 \mu\text{m}$. We decided to shift the resonance to $1.33 \mu\text{m}$, by etching 50 nm GaAs layer from the top. Our simulations predict that the resonance wavelength should shift to $1.31 \mu\text{m}$ after the deposition of the Schottky gold metal.

Chapter 4

Fabrication

Fabrication of high speed photodiodes consists of many steps, some of which are very important for high speed operation, like airpost, bridge and top DBR deposition. Airpost and bridge steps are introduced to decrease parasitic capacitance of the device and fabrication of metal-insulator-metal (MIM) capacitor. Top DBR deposition is due to the requirements of the RCE effect. With these steps, our fabrication process consists of eight steps, some of which involves two or more photolithography. Fortunately, most of the high speed photodetector fabrication process steps have already been developed by previous and present graduate students of our laboratory. We developed Schottky contact formation to $\text{Al}_x\text{Ga}_{1-x}\text{As}$ with indium-tin-oxide (ITO). We also deposited the $\text{SiO}_2/\text{Si}_3\text{N}_4$ top dielectric mirror to be used as a part of the RCE photodetector. All of the fabrication processes are made in our Advanced Research Laboratories in a Class-100 clean room environment.

4.1 Standard Processes

4.1.1 Cleaving and Wafer Cleaning

We prefer working with small samples cleaved from very expensive MBE grown wafers. Sample sizes are around 8×8 mm and the mask is 7×7 mm square. We

use a diamond tipped scribe-pen to define a line at the back of the substrate. After defining the shape of the sample, the wafer can be easily cleaved.

Every step starts with a standard cleaning process, called three solvent cleaning (TSC). Samples are immersed into the boiling trichloroethane for 2 minutes, then to acetone at room temperature for 5 minutes, and finally to boiling isopropanol for 2 minutes. Trichloroethane dissolves any possible oils, acetone dissolves organic molecules, photoresist residues and trichloroethane, and isopropanol dissolves acetone. Samples are rinsed in the deionized (DI) water flow and dried with nitrogen gun. Cleaning ends with dehydration bake at 120 °C for 2 minutes on a hot plate.

4.1.2 Photolithography

Photolithography (PL) is the name of patterning the features on to the surface of the sample. These patterning techniques involve energy-sensitive chemical substances called resist. The exposure can be done using ultraviolet (UV) light, electron beam, x-ray etc. according to the resist used. We use AZ5214E type resist which has an absorption peak around 360 nm that is ideal for UV exposure with Hg (i-line at 365 nm) lamp. Alignment is achieved by using a Karl-Suss MJB3 mask aligner.

The sample surface is first covered with an adhesion-promoter called HMDS, which provides a better adhesion of the photoresist to the surface of the sample. Then, the resist is applied on the surface. Both HMDS and resist are spun at 5000 RPM. The resultant resist thickness is around 1.3 μm . The samples are then baked at 110 °C for 55 seconds. At this point, we choose one of the following PL methods.

- **Normal Photolithography** : After pre-bake, the sample is aligned with respect to the mask. The sample is then exposed under UV-lamp for about 26 seconds with an optical power of 5.0 mW/cm² for a total dose of 130 mJ/cm².
- **Image Reversal Photolithography** : After prebake, the sample is

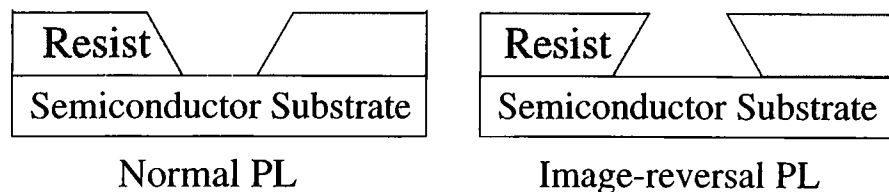


Figure 4.1: Resist profile of normal and image-reversal photolithography

aligned with respect to the image reversal mask. The sample is then exposed under UV-lamp for about 10 seconds with an optical power of 5.0 mW/cm^2 for a total dose of 50 mJ/cm^2 . Then the sample is baked at $110 \text{ }^\circ\text{C}$ for 2 minutes. After the bake, the whole sample is exposed for 30 seconds with an optical power of 5.0 mW/cm^2 for a total dose of 150 mJ/cm^2 .

For the development of the exposed samples, AZ400K developer is used with a 1:4 (Developer:H₂O) ratio. As the desired regions of the resist are etched by the developer, change in the color can be observed with naked eye. When this color change stops, sample is rinsed under DI water. After drying the sample, we check the alignment and the development. The resolution patterns must be sharp, and for a good photolithography $\sim 1\mu\text{m}$ resolution should be observable. Image reversal PL helps a lot for overcoming the lift-off problem of thick metalization. Normal PL is used for thin metalization, etch, and post step.

4.1.3 Etching

Etching is used for transforming the defined patterns by PL onto the underlying metal, semiconductor or dielectric layers, so that the desired layer is reached for the subsequent process. Etching is also used for cleaning resist, removing damaged material, polishing, removing surface oxides. Two types of etching is used in the semiconductor processes: wet and dry etching.

- **Wet Etching** : Chemical reactions that occur at the surface of the material are the main mechanisms for the wet etch. The etch mechanism of GaAs

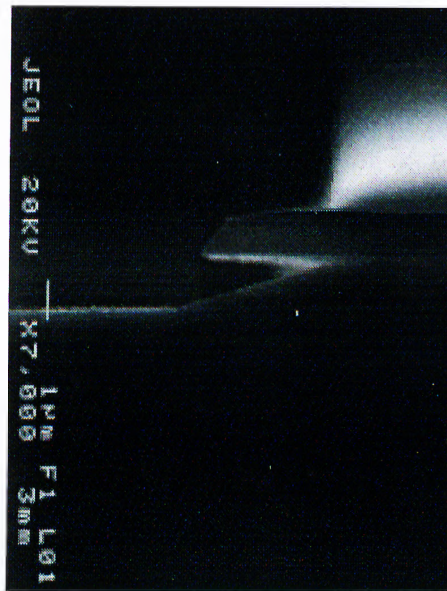


Figure 4.2: SEM image of wet-etch profile

based semiconductors, is first to oxidize the surface with an oxidizing agent, and then remove the oxidized layer with acid or base. Many etchants have been reported for etching GaAs.⁴⁴ In fact any oxidizer and oxide-dissolver combination will act as etchant. Some of them has gained popularity in the GaAs process, such as; $\text{H}_2\text{SO}_4\text{-H}_2\text{O}_2\text{-H}_2\text{O}$, $\text{HCl-H}_2\text{O}_2\text{-H}_2\text{O}$, $\text{HCl-CH}_3\text{COOH-K}_2\text{Cr}_2\text{O}_7$, $\text{Br-CH}_3\text{OH}$.⁴⁴ Dielectric materials such as SiO_2 , Si_3N_4 , TiO_2 , Al_2O_3 can be etched using hydrofluoric acid (HF), buffered HF, or phosphoric acid (H_3PO_4). HF can also used to etch ITO. Before etching, the sample is post-baked at 120°C for 1 minute to adhere the resist to the sample. The wet etch of GaAs is very anisotropic due to its crystalline structure. We use $\text{H}_2\text{O}_2\text{-NH}_3\text{-H}_2\text{O}$ (2.4:14:300) to etch GaAs, which results in an etch rate of 3.5 nm/sec at room temperature. Etch profile of this etchant system is shown in Figure 4.2, where the under-etch and the resist profile are also seen.

- **Dry Etching** : Dry etching techniques use plasma-driven chemical reactions or energetic ion beams. Some of dry etching techniques are plasma etching, reactive ion etching (RIE), reactive ion-beam etching (RIBE), sputter etching, and ion milling. Plasma etching refers to processes in which plasma generates reactive species that etch the material chemically. RIE, and RIBE are similar to plasma etching but utilize only kinetically assisted chemical etching, and this enhances directionality. Sputter etching, and ion milling are mechanical etching methods where energetic ions from the plasma or inert gases strike the surface and blast atoms away. We use ultra high vacuum (UHV) RIE machine for dry etching. With appropriate gases, dielectrics, semiconductors, resist, even metals can be etched with this system. We used O_2 gas to etch photoresist. CCl_2F_2 is used to etch SiO_2 , Si_3N_4 , and ITO.

4.1.4 Metalization

Metals are deposited onto the sample using UHV LE590 box coater. Metals in the form of solid or powder are placed into the tungsten boats. Vacuum is created inside the chamber and then metals are evaporated by passing current through the boats. Samples are placed on top of the desired boat and during the evaporation deposited metal thickness is monitored with a detector, hence metal thickness can be controlled very accurately.

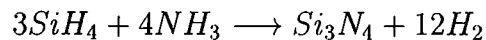
4.1.5 Annealing

Rapid thermal process (RTP) is used to heat the samples very rapidly to very high temperatures (as high as $1400\text{ }^\circ\text{C}$) to form ohmic contacts. Flash lamps are embedded into the RTP device as the heat source. Samples are heated under the radiation of these flash lamps for a certain time. We anneal the samples for 45 seconds at $450\text{ }^\circ\text{C}$. Due to high temperature ohmic metal starts to melt, and germanium (Ge) diffuses into GaAs and gallium (Ga) diffuses into the metal. The contact barrier becomes so thin that electrons can pass through that without any

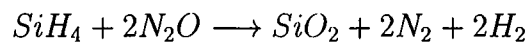
resistance.

4.1.6 Plasma Enhanced Chemical Vapor Deposition

Dielectric coatings are important for optoelectronic devices and Si based integrated circuit technology. They function as antireflection or reflection coatings, and dielectric isolation of metals. These coatings must be deposited at fairly low temperatures, so that the metal contacts are not effected. Plasma enhanced chemical vapor deposition (PECVD) allows low temperature and uniform film deposition. SiO_2 , Si_3N_4 film are deposited with PECVD in our process. We use silane (2% SiH_4 + 98% N_2), ammonia (NH_3), and N_2O for this purpose. The overall reactions would be:



and



4.1.7 Indium Tin Oxide Deposition

ITO is deposited with sputtering technique using UHV LE590 box coater. Samples are placed above the ITO target, inside the argon (Ar) plasma. Energetic Ar atoms blast ITO from the target and deposit them to the sample surface. Optical and electrical characteristics ITO layer strongly depend on the deposition rate and conditions.

4.1.8 Lift-off

After the metalization, the samples are soaked into acetone. Acetone dissolves the resist so that the metal deposited on top of the resist will be lifted-off. Only metal deposited to the openings will remain on the surface of the sample. Sometimes some part of the metal cannot be lifted-off, and ultrasound treatment has to be

applied. But this is a risky method as ultrasound may lift off other metals that should stay on top the sample.

4.2 Fabrication

4.2.1 Ohmic Contact Formation

After the PL, the sample is etched until the middle of the n+ layer ($\sim 0.50\mu\text{m}$ for NIST sample and $\sim 0.44\mu\text{m}$ for ISU sample) is reached. The overall etch is done in several steps, and at each step the etch depth is measured with DekTak stylus profilometer. After reaching the desired depth, metalization is done. Ge/Au/Ge/Au/Ni/Au layers are deposited with thicknesses of 108/102/63/236/100/2000 Angstroms, respectively. When the lift-off is completed, the samples are cleaned for the RTP anneal. RTP anneal is performed as described earlier. When observed under the optical microscope, metals exhibit Swiss-cheese like features due to the surface roughness. The ohmic quality is determined by measuring ohmic patterns with the HP4142B DC source/monitor unit.

4.2.2 Mesa Isolation

Prior to normal PL, the samples are wet-etched until the undoped layer is reached ($\sim 0.85\mu\text{m}$ for NIST sample and $\sim 0.84\mu\text{m}$ for ISU sample). All the areas except the diode active areas are etched in this step.

4.2.3 Interconnect Metalization

In order to connect the mesas to the transmission lines or microwave compatible pads, an interconnect metal layer is deposited on top of the undoped layer. Image reversal PL is done before the metalization, so that the undercut profile for an easy lift-off is obtained. First, a thin (10 nm) Ti layer is deposited to adhere the subsequent Au layer ($\sim 0.8\mu\text{m}$) to the surface.

4.2.4 Schottky Contact Formation

In our designs, we use different materials for the Schottky contact.

- **NIST sample** : Transparent ITO layer is deposited all over the sample to form the Schottky contact of our device. Sample is cleaned before the deposition, and 100 nm ITO layer is deposited with a rate of 1 Angstrom/sec using magnetron sputtering. The deposition rate and the thickness of the film is controlled during the process.
- **ISU sample** : Normal PL is applied before thin Au metalization. After the lift-off, sample is cleaned and 100 nm ITO layer is deposited as in the case of the NIST sample.

After the ITO deposition, the sample is cleaned, and image reversal Schottky PL is applied. After the development, sample is baked at 120 °C for 1 minute, and the ITO layer is etched with dilute HF (HF:H₂O = 1:80). When cleaned, the sample contains ITO on top of the active device area.

4.2.5 Dielectric Deposition

Thin (~200 nm for NIST sample, and ~280 nm for ISU sample) PECVD grown Si₃N₄ layer is deposited all over the surface of the sample. The film thickness is controlled after the deposition with an ellipsometer. Using normal PL, the nitride layer is etched away from the Schottky contact, and pad contacts. This is achieved with either wet (using dilute HF) etch or dry (RIE with CCl₂F₂ gas) etch. For both cases, it is important to stop the etch at the ITO layer as the etchants used also etch ITO. The Si₃N₄ layer functions as antireflection coating, and the dielectric slab of the MIM capacitor. It also protects Schottky layer from physical damages.

4.2.6 Airpost Formation

Before the airbridge metalization, post openings are formed with normal PL. Then the samples are hard baked at the oven at 140 °C for 30 minutes, so that

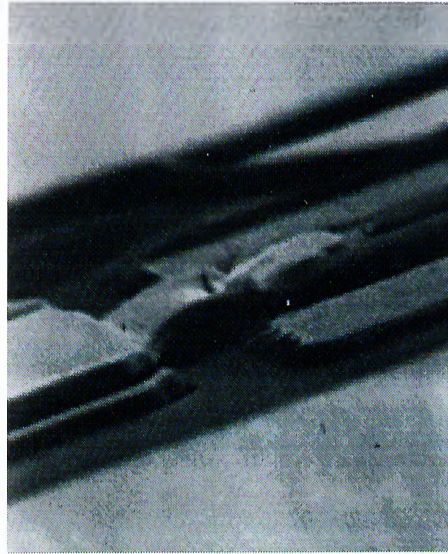


Figure 4.3: SEM photograph of an airbridge

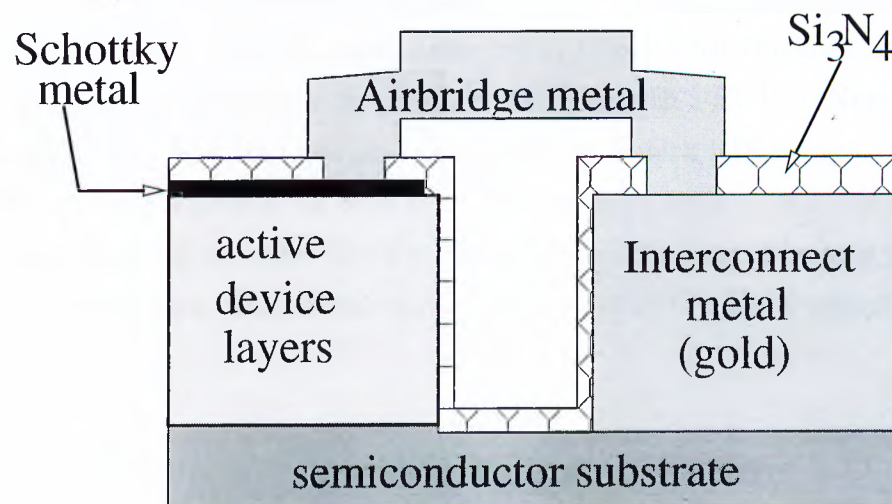


Figure 4.4: Crosssection of an airbridge

that resist doesn't dissolve in the preceding PL. After the hard bake, resist thickness is about $1.3\mu\text{m}$. O_2 RIE is applied to thin the resist down to about $0.45\mu\text{m}$, so that a $0.75\mu\text{m}$ bridge metalization will be thick enough to make the bridge.

4.2.7 Airbridge Metalization

Image reversal PL is applied for this step, and $0.75 - 0.80\ \mu\text{m}$ Ti/Au metal is deposited. Metal connects two airposts, one on the pad, and the other one on the Schottky or ohmic metal. When the resist is dissolved in the acetone, the deposited metal hangs on the air, defining an airbridge. The top metal of the MIM capacitor is also formed during this metalization. Airbridge is needed to obtain low parasitic capacitances and to carry higher currents. A connection from the surface results in higher capacitance than the airbridge. Figure 4.3 and Figure 4.4 show SEM image of an airbridge and the crosssection of an interconnect metal respectively.

4.2.8 Top Mirror Deposition

Top mirror consists of distributed Bragg reflector (DBR) which consists of $\lambda/4$ $\text{SiO}_2 - \text{Si}_3\text{N}_4$ layers. First SiO_2 and then Si_3N_4 layers with thicknesses 119/144 nm respectively, are deposited all over the sample with PECVD. Normal PL is applied after TSC, and $\text{SiO}_2 - \text{Si}_3\text{N}_4$ layers are etched with RIE using CCl_2F_2 gas. Wet etch with HF can not be used here because etch rate of Si_3N_4 is about 20 times higher than SiO_2 . After the top mirror deposition, our detectors are ready for the measurements. Top mirror is deposited only to the NIST sample.

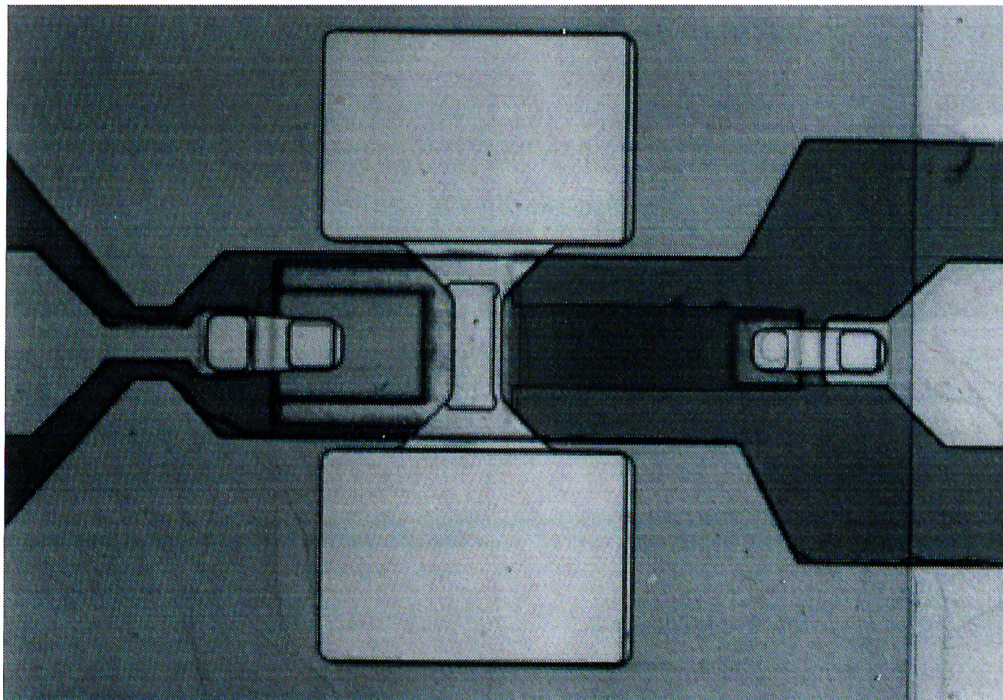


Figure 4.5: Photograph of complete device

Chapter 5

Measurements

After the fabrication, measurements are done to make the characterization of our photodiodes. Current-voltage (IV) measurements are performed first, as it is an important performance indicator. This is followed by the quantum efficiency (QE) and high-speed measurements to determine the performance of the diodes. Current-voltage and quantum efficiency measurements are performed in Bilkent University. High-speed measurements are done in Boston University.

5.1 IV Measurements

We used an HP 4142B Modular DC Source/Monitor analyzer in our IV measurements. We first check the diode characteristics around zero bias voltage. We then increase the forward bias to get the turn-on voltage. Using the measurements at this voltage range, we determine the Schottky barrier height. Once the forward characteristics are observed, we increase the reverse bias to measure the breakdown voltage. A probe station is used to make contact to the pads.

Figure 5.1 shows the IV characteristics of 28×18 , 120×100 , and $150 \times 150 \mu m^2$ area photodiodes from the ISU sample. Dark current of our devices at -1 V bias is around 160 nA. Using forward characteristics at low voltages (< 1 V), we found that Schottky barrier height (ϕ_B) is 0.8 eV. Typical breakdown voltage for

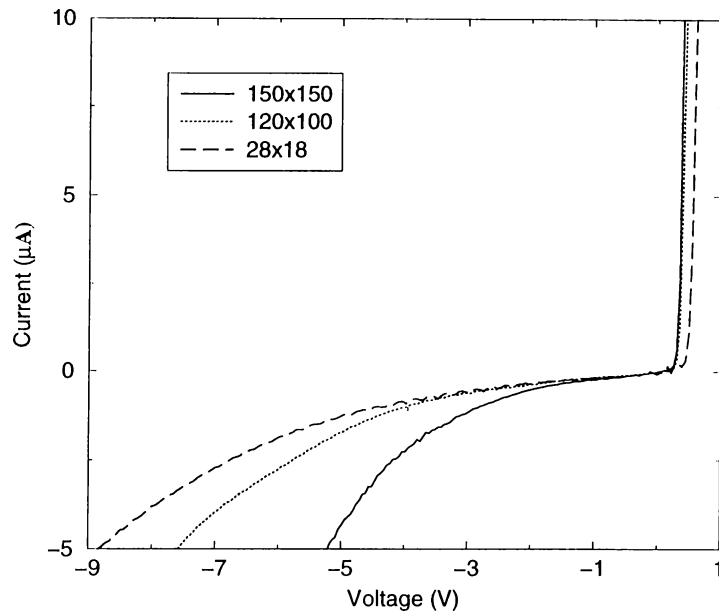


Figure 5.1: Current-Voltage characteristics of ISU sample

the NIST sample is -8 V.

5.2 Quantum Efficiency Measurements

QE measurements were made with an experimental setup shown in Figure 5.2. A tungsten-halogen lamp is used as light source. Monochromator takes light from this lamp and gives monochromatic light as output. This light is chopped and coupled to a $62.5 \mu\text{m}$ diameter multimode fiber. Chopped light is delivered to the device by a lightwave fiber probe, and electrical contacts are made on the probe station which is also used in IV measurements. Chopping frequency and generated photocurrent are sent to the lock-in amplifier which displays the phase and the amplitude of the current. The power spectrum was measured by a calibrated optical powermeter.

Large area diodes were chosen for the quantum efficiency measurements to ensure that all light coming out from the fiber is coupled to the device.

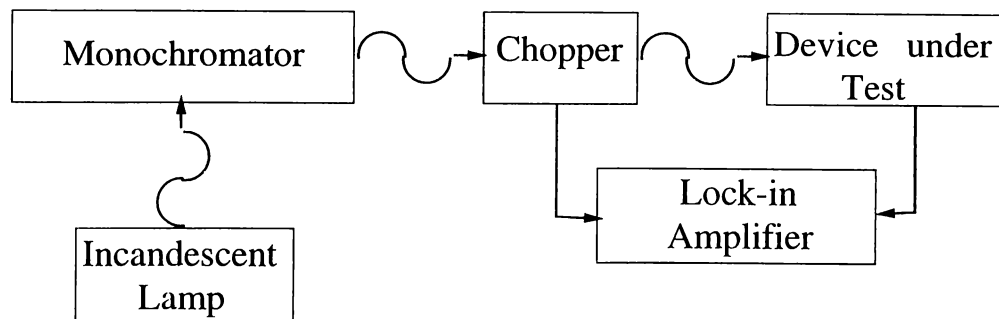


Figure 5.2: Simple diagram of quantum efficiency setup

5.2.1 NIST Sample

According to our simulations, we were expecting the peak quantum efficiency at 840 nm. To see the spectral behavior of the quantum efficiency, measurements are done from 750 nm to 900 nm. Top DBR is grown pair-by-pair to see the increase in the quantum efficiency, and the correlation between theory and experiment. Figure 5.3 shows our results. Before top DBR deposition, the measured peak quantum efficiency was 33%, while the calculations predicted 43%. Depositing top mirror pair-by-pair, the value increased to 41%, 48%, 54%, 58%, 59%, for 1 to 5 pair of $\text{Si}_3\text{N}_4/\text{SiO}_2$. The maximum peak efficiency measured is 59% with 5 pair top DBR, where theoretically predicted peak value is 84%. Each time we deposit $\text{Si}_3\text{N}_4/\text{SiO}_2$ pair on top of our structure, we go over the last step of our process. So we add non-perfect, rough interfaces to the top DBR, which decreases the coupling of light into the cavity. Although the discrepancy between our experimental and theoretical results is quite large, a nearly parallel enhancement as a function of DBR pair number is observed. Moreover, our experimental results confirmed that the optimum efficiency condition, $R_{top} = R_{bot}e^{-2\alpha d}$ was satisfied with 5 pair of top DBR. Full width at half max (FWHM) of the resonant peak decreased from 30 nm to 10 nm, while at the same time wavelength selectivity increased by a factor of ~ 8 which are in good agreement with our theoretical expectations.

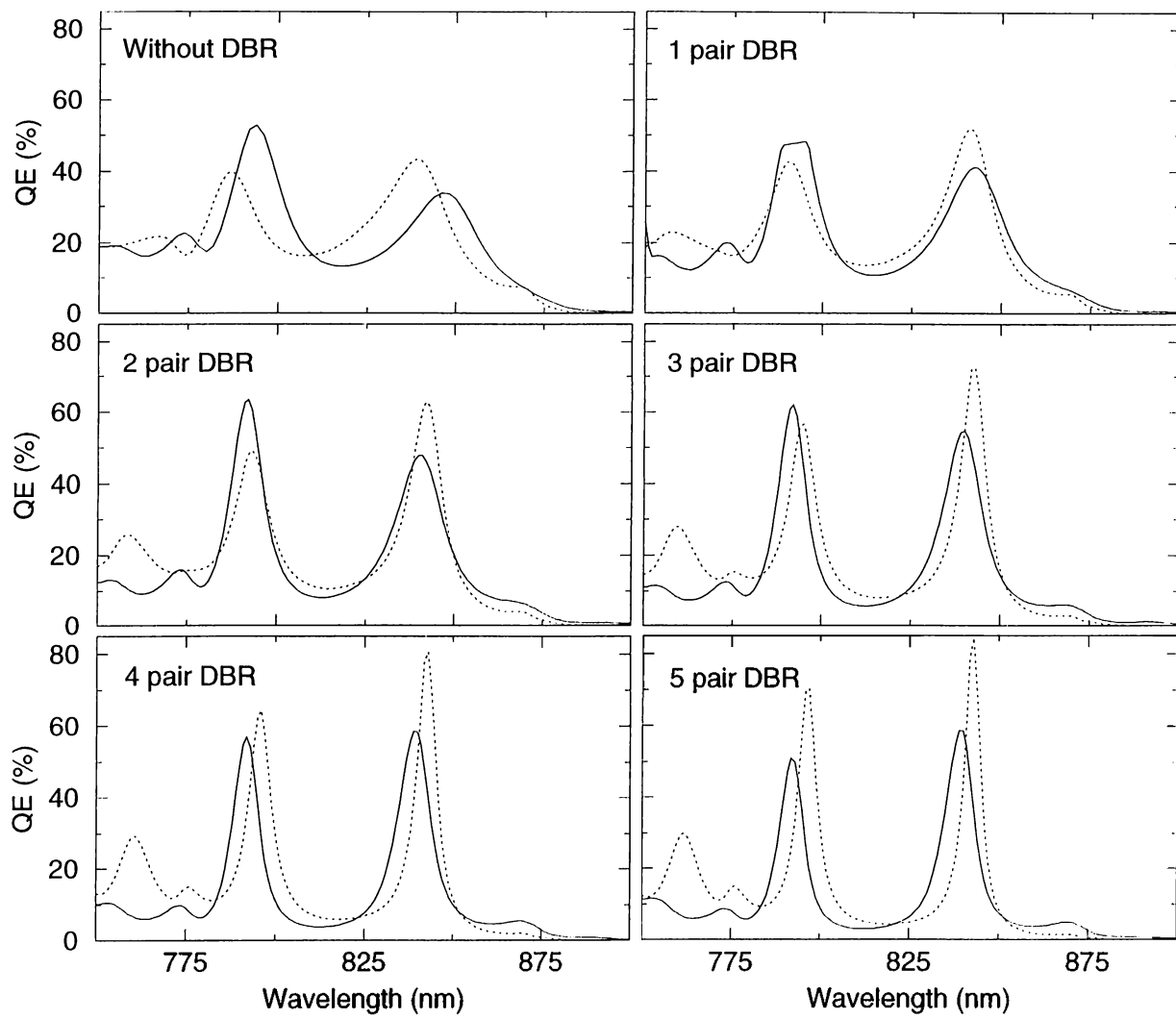


Figure 5.3: Experimental (solid line) and theoretical (dotted line) Quantum Efficiency of NIST sample for different top DBR pair number

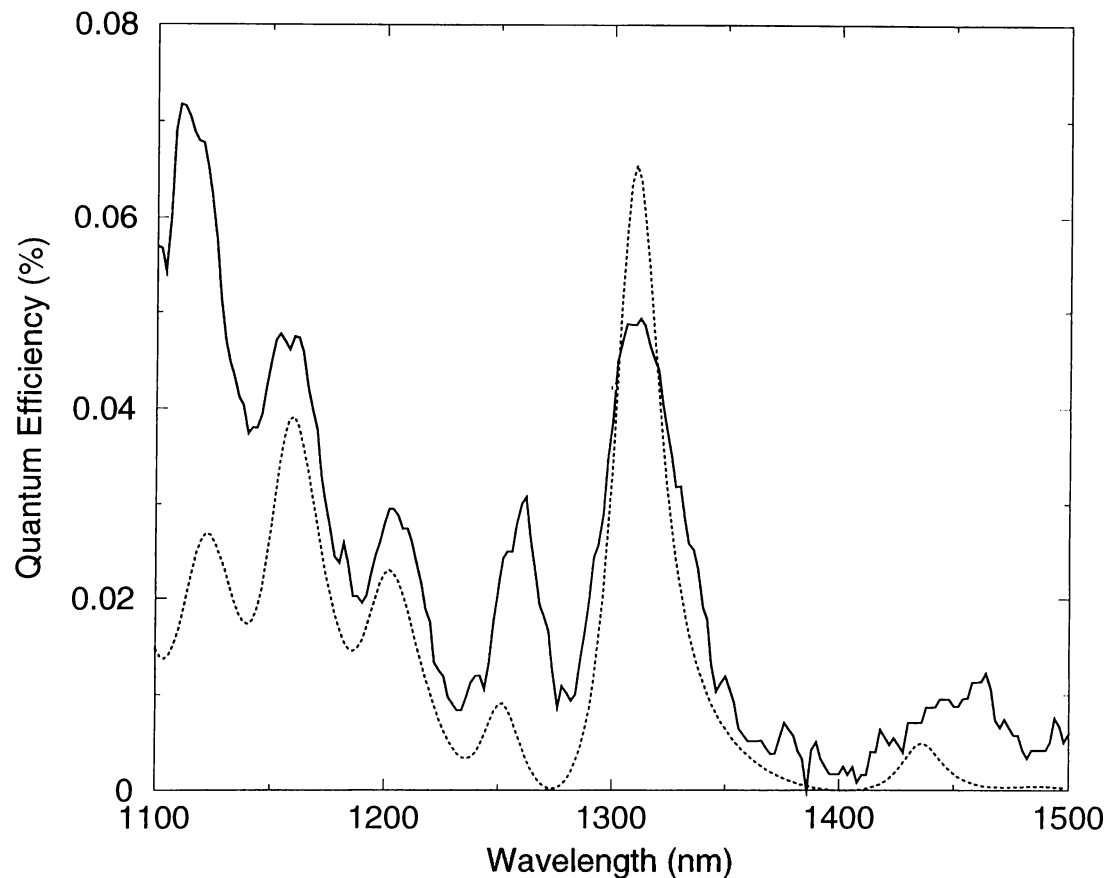


Figure 5.4: Experimental (solid line) and theoretical (dotted line) Quantum Efficiency of ISU sample

5.2.2 ISU Sample

Quantum efficiency of photodetectors is proportional to the absorbed power in the gold Schottky layer and the frequency of the incoming photons. For the wavelengths smaller than the cut-off wavelength:

$$\eta \propto P_{abs}(\lambda) \times \left(\frac{1}{\lambda} - \frac{1}{\lambda_0} \right)^2 \quad (5.1)$$

The cut-off wavelength is determined from the Schottky barrier height. From our current voltage measurements, we determined the cut-off wavelength (λ_0) to be 1530 nm. We used RCE to increase the power absorbed (P_{abs}) in the gold

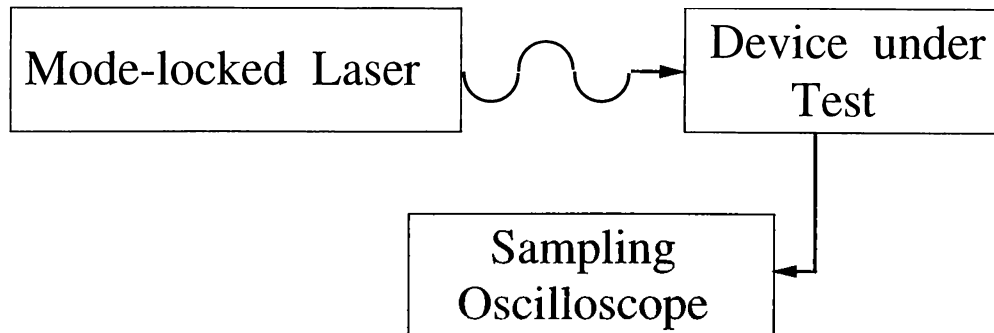


Figure 5.5: Simple diagram of high speed setup

Schottky layer. Due to the wavelength selectivity of the RCE effect, we expected peaks at the resonance wavelengths. We measured the quantum efficiency from 1100 nm to 1500 nm. The theoretical and experimental results are presented in Figure 5.4, where a good agreement between our results can be seen. The resonance peak also shifted to 1312 nm as we predicted before the fabrication. The quantum efficiency at 1312 nm is 0.05%. FWHM of this peak is 40 nm.

5.3 High-Speed Measurements

High speed measurements were made with a 1 psec FWHM optical pulses obtained from a Ti-Sapphire laser tuned to the peak of the quantum efficiency. Optical pulses from the laser were coupled to a single-mode fiber, and the pulses from the fiber were coupled to the devices. A simple diagram of the setup is shown at Figure 5.3. Temporal response of the small area diodes are measured with 50 GHz sampling scope.

As expected, the best results, i.e. fastest responses are measured from small area diodes. Large area diodes are RC-limited, whereas small area diodes are transit time limited.

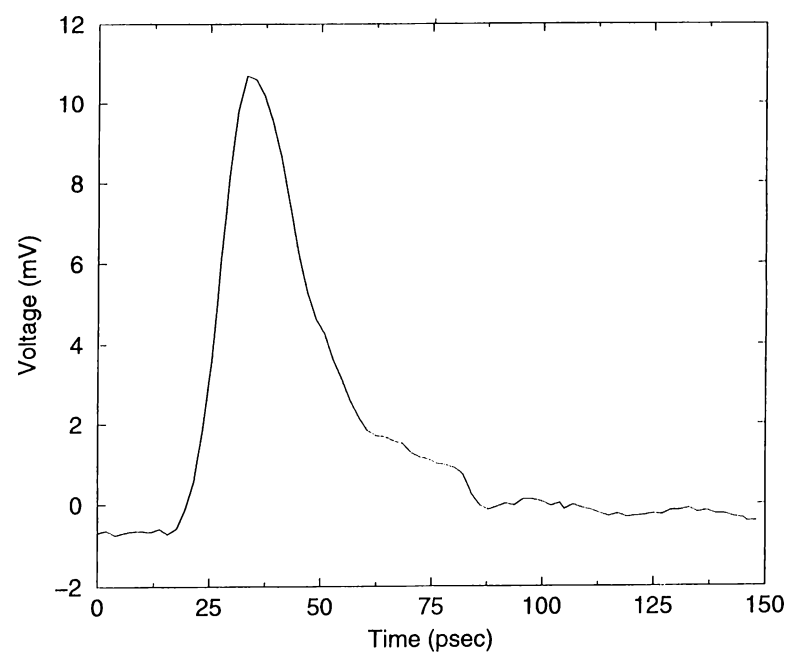


Figure 5.6: Response of the NIST sample

5.3.1 NIST Sample

Figure 5.6 shows the response of $112 \mu\text{m}^2$ area device. The measured photodiode output has a 20 psec FWHM at 3 V bias. At zero bias, the device has FWHM of 35 psec. We expected better results if we were able to apply 4-5 volts bias, but the leakage in device capacitors prevented us from going beyond 3 V bias. The Fourier transform of this data has a 3-dB bandwidth of ~ 20 GHz. Bandwidth efficiency product (BWE) is ~ 12 GHz.

5.3.2 ISU Sample

After the wavelength tuning, the length of the n- region decreased to $0.15 \mu\text{m}$. According to the transit time calculations, the speed of our device should be $f_{tr}^{3-dB} \simeq 300$ GHz. But due to thin depletion layer, our devices are RC time limited. According to our calculations, the speed of $100 \mu\text{m}^2$ devices should be $f_{RC}^{3-dB} \simeq 50$ GHz.

Chapter 6

Achievements and Future Directions

In the previous chapters, we presented our work on design, fabrication, and characterization of high performance GaAs/AlGaAs based RCE photodetectors operating in the first and second optical communication window. We began our work with theoretical simulations, that we use in the design of RCE photodiodes. The main effort was devoted to the fabrication of MBE grown samples and characterization of the fabricated photodiodes. We introduced top DBR deposition and ITO deposition to the current process.

Reflectivity and quantum efficiency measurements have shown reasonable agreements with our theoretical predictions. The NIST sample showed 59% maximum quantum efficiency. The discrepancy between the measurements and the simulations can be explained with non-perfect interfaces of the DBR pairs. Due to the current leakage in the MIM capacitors, we could not apply high biases to our devices. The speed of our devices at 3 V bias is 20 GHz. After fabricating NIST structure, we expect to be able to bias to higher voltages and measure the full performance of our photodiodes.

Due to the lack of a high speed light source at 1.3 μm , we were not able to measure the high speed characteristics of our photodetectors. We plan to perform high-speed measurements by collaborating with researchers in Bilkent Electrical

and Electronic Engineering Department. We predict a 50 GHz bandwidth from ISU samples. Top DBR deposition to this sample is also expected to increase the quantum efficiency. Also the increase in the quality factor of the cavity will decrease the FWHM of the peak. This reduction will increase the wavelength selectivity.

The main effort will be devoted to the development of RCE photodiodes operating at 1.3 μm and 1.55 μm . High performance RCE photodiodes are promising detectors for high bit-rate optical communication. Their wavelength selectivity can be used for the WDM applications. We will develop the fabrication of several long-wavelength material systems (InP /InGaAs/InAlAs/InAs/InSb/GaSb), and low temperature grown GaAs. For high bandwidth measurements (>100 GHz), we are considering electro-optic sampling, photoconductive sampling, and two laser heterodyne beating measurements.

Bibliography

- [1] Giovanni Cancellieri and Franco Chiaraluce, Recent Progress in Fibre Optics, Prog. Quant. Elect. **18**, 39, (1994)
- [2] S. Y. Wang and D. M. Bloom, 100 GHz bandwidth planar GaAs Schottky photodiode, Electron. Lett. **19**, 554, (1983)
- [3] E. Ozbay, K. D. Li, and D. M. Bloom, 2.0 psec GaAs monolithic photodetector and all electronic sampler, IEEE Photonics Tech. Lett. **3**, 570, (1991)
- [4] K. D. Li, A. S. Hou, E. Özbay, B. A. Auld, and D. M. Bloom, 2-picosecond, GaAs photodiode optoelectronic circuit for optical correlation applications, Appl. Phys. Lett. **61**, 3104, (1992)
- [5] Y. G. Wey, K. S. Giboney, J. E. Bowers, M. J. Rodwell, P. Silvestre, P. Thiagarajan, and G. Y. Ribbons, 110 GHz GaInAs/InP p-i-n Photodiodes with Integrated Bias Tees and Matched Resistors, IEEE Photonics Tech. Lett. **5**, 1310, (1993)
- [6] N. Bıyıklı, Design, Fabrication and Characterization of High Performance Resonant Cavity Enhanced Photodetectors, Bilkent University Ms. Thesis, September 1998
- [7] P. Kordos, A. Forster, M. Marso, and F. Ruders, 550 GHz bandwidth photodetector on low-temperature grown molecular-beam epitaxial GaAs, Electron. Lett. **34**, 119, (1998)

- [8] B. L. Sharma, *Metal-Semiconductor Schottky Barrier Junctions and Their Applications*, (Plenum Press, 1984)
- [9] H. A. Bethe, *Theory of the Boundary Layer of Crystal Rectifiers*, MIT Radiat. Lab. Rep. **43-12**, (1942)
- [10] W. Schottky, *Halbleitertheorie der Sperrschicht*, *Naturwissenschaften*, **26**, 843, (1938)
- [11] C. R. Crowell and S. M. Sze, *Current Transport in Metal-Semiconductor Barriers*, *Solid State Electron*, **9**, 1035, (1966)
- [12] S. M. Sze, *Physics of Semiconductor Devices*, (John Wiley & Sons, 1981)
- [13] E. Özbay, *Breaking World Records in High Speed Microelectronics*, Stanford University Ph.D. Thesis, February 1992
- [14] Bor-Yeu Tsaur, Melanie M. Weeks, R. Tubiano, Paul W. Pellegrini, T.-R. Yew, *IrSi Schottky-Barrier Infrared Detectors with 10- μ m Curoff Wavelength*, *IEEE Elect. Dev. Lett.*, **9**, 650, (1998)
- [15] R. H. Fowler, *The Analysis Of Photoelectrical Sensitivity Curves For Clean Metals At Various Temperatures*, *Phys. Rev.*, **38**, 45, (1931)
- [16] G. Gigli, M. Lomascolo, M. De Vittorio, R. Cingolani, A. Cola, F. Quaranta, L. Sorba, B. Mueller, A. Franciosi, *Direct assesment of tunable Schottky barriers by internal photoemission spectroscopy*, *Appl. Phys. Lett.*, **73**, 259, (1998)
- [17] V. E. Vickers, *Model of Schottky Barrier Hot-Electron-Mode Photodetection*, *Appl. Opt.*, **10**, 2190, (1971)
- [18] Vikram L. Dalal, *Simple Model for Internal Photoemission*, *J. of Appl. Phys.*, **42**, 2274, (1971)

- [19] Eric Y. Chan, Howard C. Card, and Malvin C. Teich, internal Photoemission Mechanisms at Interfaces Between Germanium and Thin Metal Films, *IEEE J. of Quantum Electron.*, **16**, 373, (1980)
- [20] M. Selim Ünlü, Samuel Strite, Resonant cavity enhanced photonic devices, *J. Appl. Phys.*, **78**, 607, (1995).
- [21] B. Corbett, L. Considine, S. Walsh and W. M. Kelly, Narrow bandwidth long wavelength resonant cavity photodiodes, *Electron. Lett.* **29**, 2148, (1993)
- [22] A. Srinivasan, S. Murtaza, J. C. Campbell and B. G. Streetman, High quantum efficiency dual wavelength resonant-cavity photodetector, *Appl. Phys. Lett.* **66**, 535, (1995)
- [23] Ekmel Özbay, İbrahim Kimukin, Necmi Bıyıklı, Orhan Aytür, Mutlu Gökavas, Gökhan Ulu, M. Selim Ünlü, Richard P. Mirin, Kris A. Bertness, David H. Christensen, High-speed >90% quantum-efficiency p-i-n photodiodes with a resonance wavelength adjustable in the 795-835 nm range, *Appl. Phys. Lett.* **74**, 1072, (1999)
- [24] K. A. Anselm, S. S. Mustaza, C. Hu, H. Nie, B. G. Streetman, and J. C. Campbell, A Resonant-Cavity, Separate-Absorption-and-Multiplication, Avalanche Photodiode with Low Excess Noise Factor, *IEEE Electron Dev. Lett.* **17**, 91, (1997)
- [25] H. Nie, A. Anselm, C. Hu, S. S. Mustaza, B. G. Streetman, and J. C. Campbell, High-speed resonant-cavity separate absorption and multiplication avalanche photodiodes with 130 GHz gain-bandwidth product, *Appl. Phys. Lett.* **70**, 161, (1997)
- [26] M. Razeghi and A. Rogalski, Semiconductor ultraviolet detectors, *J. Appl. Phys. Rev.* **79**, 7433, (1996).
- [27] Thomas N. Casselman, State of Infrared Photodetectors And Materials, in *Photodetectors: Materials and Devices II*, Gail J. Brown, Manijeh Razeghi, Editors, Proceeding of SPIE vol 2999, 2-10 (1997)

- [28] R. Le Dantec, T. Benyattou, G. Guillot, A. Spisser, C. Seassal, J. L. Leclercq, P. Viktorovitch, D. Rondi, and R. Blondeau, **Tunable Microcavity Based on InP-Air Bragg Mirrors**, *IEEE J. of Selected Topics in Quantum Electron.*, **5**, 111, (1999)
- [29] G. Kinsley, C. Lenox, H. Nie, J. C. Campbell and B. G. Streetman, **Resonant Cavity Photodetector with Integrated Spectral Notch Filter**, *IEEE Photonics Technol. Lett.*, **10**, 1142, (1998)
- [30] M. D. Learmouth, N. P. Hewett, I. Reid, M. J. Robertson, **Integrated Dielectric Wavelength Filters on InGaAs PIN Photodetectors**, *Electron. Lett.*, **26**, 576, (1990)
- [31] T. Baba, S. Tamura, Y. Kokubin, and S. Watanabe, **Monolithic Integration of Multilayer Filter on Vertical Surface of Semiconductor Substrate by a Bias-Sputtering Technique**, *IEEE Photonics Technol. Lett.*, **2**, 191, (1990)
- [32] A. Osinsky, S. Gangopadhyay, R. Gaska, B. Williams, M. A. Khan, D. Kuksenkov, H. Temkin, **Low noise p- π -n GaN ultraviolet photodetectors**, *Appl. Phys. Lett.*, **71**, 2334, (1997)
- [33] A. Osinsky, S. Gangopadhyay, J. W. Yang, R. Gaska, D. Kuksenkov, H. Temkin, I. K. Shmagin, Y. C. Chang, J. F. Muth, R. M. Kolbas **Visible-blind GaN Schottky barrier detectors grown on Si(111)**, *Appl. Phys. Lett.*, **72**, 551, (1998)
- [34] Q. Chen, J. W. Wang, A. Osinsky, S. Gangopadhyay, B. Lim, M. Z. Anwar, D. Kuksenkov, H. Temkin, **Schottky barrier detectors on GaN for visible-blind ultraviolet detection**, *Appl. Phys. Lett.*, **70**, 2277, (1997)
- [35] I. K. Sou, C. L. Man, Z. H. Ma, Z. Yang, G. L. K. Wong, **High performance ZnTe photovoltaic visible-blind ultraviolet detectors**, *Appl. Phys. Lett.* **71**, 3847, (1997).

- [36] Ekmel Özbay, M. Saiful Islam, Bora Onat, Mutlu Gökkavas, Orhan Aytür, Gary Tuttle, Elias Towe, R. H. Herderson, M. Selim Ünlü, Fabrication of High-Speed Resonant Cavity Enhanced Schottky Photodiodes, *IEEE Photon. Technol. Lett.*, **9**, 672, (1997)
- [37] B. M. Onat, M. Gökkavas, E. Özbay, E. P. Ata, E. Towe, M. S. Ünlü, 100-GHz Resonant Cavity Enhanced Schottky Photodiodes, *IEEE Photon. Technol. Lett.*, **10**, 707, (1998)
- [38] H. Kim, A. Piqué, J. S. Horwitz, H. Mattoussi, H. Murtaza, Z. H. Kafafi, C. B. Chrisey, Indium tin oxide thin films for organic light-emitting devices, *Appl. Phys. Lett.*, **74**, 3444, (1999)
- [39] W. A. Wohlmuth, J. W. Seo, P. Fay, C. Caneau, I. Adesida, A high-speed ITO-InAlAs-InGaAs Schottky-barrier Photodetector *IEEE Photon. Technol. Lett.*, **9**, 1388, (1997)
- [40] D. G. Parker, Use Of Transparent Indium Tin Oxide To Form A Highly Efficient 20 GHz Schottky Barrier Photodiode, *Electron. Lett.*, **21**, 778, (1985)
- [41] D. G. Parker, P. G. Say, A. M. Hansom, 110 GHz High-Efficient photodiodes Fabricated From Indium Tin Oxide/GaAs, *Electron. Lett.*, **23**, 527, (1987)
- [42] D. G. Parker, The Theory, Fabrication and Assesment of Ultra High Speed Photodiodes, *GEC journal of Research*, **6**, 106, (1988)
- [43] Wie Gao *et al.*, Transparent and opaque Schottky contacts on undoped $\text{In}_{0.52}\text{Al}_{0.48}\text{As}$ grown by molecular beam epitaxy , *Appl. Phys. Lett.* **66**, 3471, (1995).
- [44] Ralph Williams, *Modern GaAs Processing Methods*, (Artech House, 1990)